Graphical Abstract

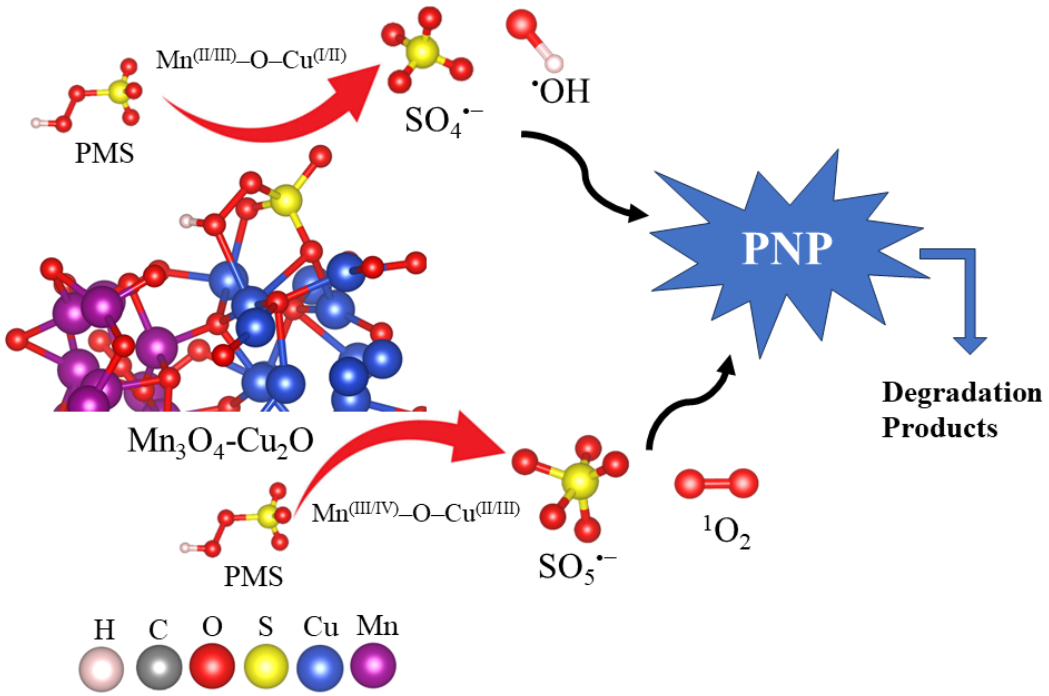


A possible reaction mechanism over the $Mn_3O_4$-$Cu_2O$/PMS system for PNP degradation.

# Synergistic degradation of *p*-nitrophenol using peroxymonosulfate activated with a bimetallic $Mn_3O_4$–$Cu_2O$ catalyst: Investigation of strong interactions between metal oxides

Qiaohui Gao [a, b], Habib Ullah [c], Zidong Ming [a], Shuaiqi Zhao [a], Aihua Xu [a], Xiaoxia Li [a, *], Aimal Khan [a, *]

[a] School of Chemistry and Chemical Engineering, Wuhan Textile University, Wuhan 430200, China.

[b] Hubei Provincial Engineering Laboratory for Clean Production and High Value Utilization of Bio-Based Textile Materials, Wuhan Textile University, Wuhan 430200, PR China.

[c] Department of Engineering, Faculty of Environment, Science and Economy, University of Exeter, United Kingdom.

***Corresponding author:** lixxwh@163.com (X. Li); aimalkhan@wtu.edu.cn (A. Khan)

## Abstract

The use of efficient, eco-friendly catalysts is essential for activating peroxymonosulfate (PMS) to degrade organic contaminants in aqueous media. In this study, we developed a novel approach to fabricating bimetallic MnCu catalysts (Mn:Cu molar ratios: 10:1, 5:1, 3:1, and 2:1) comprising tetragonal $Mn_3O_4$ and cubic $Cu_2O$. MnCu-5:1 exhibited superior catalytic activity for the degradation of *p*-nitrophenol (PNP) using PMS because of the synergistic interplay between Mn and Cu. Experimental and density functional theory (DFT) calculation data revealed that the mixed valence states and strong interactions between Mn and Cu in the MnCu-5:1 system increased the electron transfer efficiency and promoted electron transfer to PMS. The results of quenching experiments elucidated a primary radical mechanism and minor nonradical pathway for the PNP degradation over the MnCu-5:1/PMS system. DFT calculations confirmed a relatively high adsorption energy of the $Mn_3O_4$–$Cu_2O$ (MnCu) composite, indicating enhanced catalytic performance. The superior reactivity of the composite was verified by analyzing its density of states and electrostatic difference potential. Our findings offer fresh perspectives for harnessing the synergistic potential of less toxic mixed metal oxides for controlling catalytic properties and help achieve a better understanding of the activation mechanism for contaminant degradation over MnCu catalysts.

**Keywords:** peroxymonosulfate, organic pollutant, Mn and Cu catalysts, bimetallic catalyst, synergistic effect

## 1. Introduction

Harmful contaminants generated by industries, hospitals, and households are

discharged into the environment, thereby damaging both the ecosystem and human health [1,2]. Conventional wastewater treatment methods, such as biological processes, filtration membranes, and adsorption, cannot effectively remove all refractory organic contaminants from water bodies [3,4]. Hence, developing environmentally friendly, cost-effective, and high-efficiency methods for removing organic contaminants from water bodies is an important task. A peroxymonosulfate (PMS)-based advanced oxidation process for water and wastewater treatment has garnered considerable attention in research interest of its high efficiency and simple experimental setup. In addition, PMS produces different reactive oxygen species (ROS), such as $SO_4^{\bullet-}$, •OH, and singlet oxygen ($^1O_2$), for the degradation of refractory organic contaminants in wastewater [5,6]. The redox potential of $SO_4^{\bullet-}$ used for degrading contaminants is 2.5–3.1 V, and that of •OH is 2.7 V [2,7]. The reaction between $SO_5^{\bullet-}$ and PMS generates $^1O_2$ species, which can effectively degrade organic contaminants [5,8].

Recently, various Co-based catalysts and their hybrids have been synthesized to activate PMS and generate radicals for degrading organic contaminants [9,10]. However, Co-based catalysts are unsuitable for PMS activation because they release toxic Co ions, which are harmful to the environment [11]. Thus, inexpensive catalysts with low toxicity, high stability, and high efficiency are required to degrade organic contaminants using PMS.

Mn oxides ($Mn_xO_y$) have attracted significant attention as inexpensive catalysts that are abundant in soil [12]. In contrast to Co-based catalysts, Mn oxide-based catalysts are less toxic to the environment [11,12]. Mn predominantly exists in three oxidation states:

Mn (II), Mn (III), and Mn (IV), and their redox cycle proceeds via an electron-transfer mechanism [13]. Recent studies have shown that Mn oxides, including $MnO_2$, $Mn_2O_3$, and $Mn_3O_4$, are highly efficient catalysts for PMS activation [13–16]. However, $Mn_3O_4$ exhibits sluggish catalytic performance as compared with those of other $Mn_xO_y$ ($MnO_2$ and $Mn_2O_3$) PMS activators [16,17]. Furthermore, the structural characteristics of $Mn_3O_4$ can influence its catalytic activity [18,19]. For instance, $Mn_3O_4$ hierarchical porous materials are significantly more efficient at activating PMS for phenol oxidation as compared with their nanoparticle and nanorod counterparts [19].

Cu traces are intrinsically present in soil and can activate PMS and oxidize target contaminants [20]. Cu oxide (CuO and $Cu_2O$) catalysts have also been investigated previously for PMS activation. For instance, a CuO/PMS system degraded 2,6-dichlorophenol [21]. The structural properties of $Cu_2O$ strongly influence its catalytic activity, and its cubic crystal phase exhibits superior catalytic activity in specific reactions. For example, cubic $Cu_2O$ demonstrated a higher catalytic activity towards bisphenol A (BPA) degradation in the presence of PMS as compared with those of its rhombic dodecahedral and octahedral counterparts [22]. $CuMnO_2$ and $Ag_2Cu_2O_3$ exhibited superior performance during PMS activation as compared with that of CuO because PMS easily oxidizes Cu(I) to Cu(II) to generate radicals for the degradation of organic pollutants [23,24]. In addition, $CuFeO_2$ efficiently activated PMS owing to the low valence of Cu(I), which resulted in the generation of a sufficient amount of $SO_4^{\bullet -}$ species [25]. However, in most cases, Cu-based catalysts exhibit poorer catalytic performance for degrading organic contaminants than those of $Co_3O_4$, and $MnO_2$, and

$Mn_2O_3$ [17]. For example, CuO degraded only 10% and 12.5% of phenol and sulfamethazine in the PMS system, respectively [17,26]. In addition, the application of the CuO/PMS system for degrading organic contaminants is limited because of the following drawbacks: (i) low catalytic efficiency owing to the difficulty of valence cycling in the presence of PMS and (ii) low stability caused by the high leaching degree of Cu ions. Thus, the demand for efficient and stable bimetallic Cu-based catalysts for PMS activation is continuously increasing.

Bimetallic Cu-based catalysts demonstrate excellent performance and high stability during PMS activation owing to the synergistic interactions between the two metal species. For example, CuCo@$MnO_2$ degraded 100% of phenol, whereas Co@$MnO_2$ and Cu@$MnO_2$ degraded only 61% and 47% of phenol, respectively [9]. $CuFeO_2$ demonstrated a higher catalytic activity than those of $Cu_2O$ and $Fe_3O_4$ for BPA degradation in the PMS system [25]. Furthermore, the $CuMnO_2$ catalyst outperformed CuO and $MnO_2$ during PMS activation [23]. $CuMnO_2$ promoted the redox cycle between Cu and Mn through a synergistic effect. Moreover, the presence of Mn in the catalyst introduced new adsorption sites, which increased its overall reactivity [27]. The $CuCo_2O_4$/PMS system degraded 87.2% of organic compounds in water, whereas $Co_3O_4$ and CuO catalysts degraded only 51.1% and 12.5% of organic compounds, respectively [26]. Thus, synergistic effects can enhance the catalytic efficiency and physicochemical properties of the catalyst. Bimetallic transition metal catalysts with improved redox properties are generally favored because of the efficient electron transfer between different transition metals [28]. In addition, the tunable surface properties of such mixed

metal oxide catalysts endow them with high catalytic efficiency and potential applicability in green processes. Thus, bimetallic Cu-based compounds are promising catalysts for the degradation of organic contaminants.

This paper reports the development of an efficient heterogeneous catalyst composed of $Mn_3O_4$ and $Cu_2O$ oxides owing to their synergistic effect on PMS activation and contaminant degradation and describes its catalytic properties. First, MnCu oxides with various Mn:Cu ratios (MnCu-2:1, MnCu-3:1, MnCu-5:1, and MnCu-10:1) were synthesized via a simple precipitation process, and their catalytic properties were compared. Subsequently, the PMS activation mechanism was examined using the optimal catalyst, MnCu-5:1, to elucidate the role of radicals in contaminant degradation. In addition, the degradation of organic contaminants and effects of various factors (e.g., pH, anion type, and humic acid (HA) content) on this process were investigated using the MnCu-5:1/PMS system. The MnCu composite catalyst exhibited enhanced catalytic activity and stability owing to the synergistic interaction between Cu and Mn, which facilitated the electronic transfer between the two metals. Furthermore, the combination of Cu and Mn oxides produced a synergistic effect that enhanced the catalyst conductivity and electrochemical performance. This work describes a significant advancement in the physical properties of bimetallic catalysts as compared with those of monometallic alternatives, offering a promising avenue for the development of sustainable catalytic processes [9,26,28]. The environmentally friendly properties of the MnCu catalyst further increase its green chemistry application potential.

## 2. Materials and methods

## 2.1. Reagents

The chemicals used to prepare the catalysts and conduct experimental analyses are described in Supporting Information (Text S1).

## 2.2. Material synthesis

MnCu catalysts with different Mn:Cu ratios were synthesized using a precipitation method. First, 40 mmol of $MnSO_4$ and 8 mmol of $Cu(NO_3)_2 \cdot 3H_2O$ were dissolved in 250 mL of deionized water. Subsequently, a NaOH (0.64 mol/L) solution used as the precipitating agent was slowly added to the metal ion solution under magnetic stirring, and the resulting mixture was stirred continuously for 3 h. Thereafter, the mixture was centrifuged, and the precipitate was collected, washed several times with deionized water, and dried at 80 °C overnight. The sample obtained after calcining the precipitate in a muffle furnace at 250 °C for 4 h was crushed and ground into a powder. MnCu catalysts with Mn:Cu molar ratios of 10:1, 5:1, 3:1, and 2:1 were prepared by varying the amounts of the $MnSO_4$ and $Cu(NO_3)_2 \cdot 3H_2O$ precursors. Pure $Mn_3O_4$ was obtained via the same method, and commercial $Cu_2O$ was used in all experiments.

## 2.3. Catalyst characterization

Several analytical techniques were used to characterize the fabricated transition metal-based catalysts. X-ray diffraction (XRD; BV Empyrean, PANalytical; wavelength ($\lambda$): 1.5405 Å) was performed to determine their structure and crystallinity. Transmission electron microscopy (TEM; Tecnai G20, USA) and scanning electron microscopy (SEM; FEI Nova Nano) were utilized to determine surface morphologies. Catalyst surface areas were measured by the Brunauer–Emmett–Teller (BET) method (BET;

BEL Master Ver. 7 (for max/maxII), Japan). A Thermo Scientific DXR (XS 11638, USA) Raman spectroscopy system was employed to record catalyst Raman spectra with a 532-nm wavelength laser. The valence states and compositions of the catalysts were determined via X-ray photoelectron spectroscopy (XPS; GENESIS, EDAX, USA).

### 2.4. Experimental methods

Various degradation tests were performed using a 50 μM solution (organic contaminant) in a 50-mL conical flask containing PMS (0.65 mM) and 0.01 g of a studied catalyst under magnetic stirring at 200 rpm. The reaction temperature was maintained at 25 °C during the entire experiment. At specified time points (2.5 and 5 min), 2 mL of the sample was removed from the reaction mixture, and the amount of the organic contaminant in the sample was determined. Scavenging experiments were conducted using methanol (MeOH), *tert*-butyl alcohol (TBA), and β-carotene under the same reaction conditions. Furthermore, the effects of different anions ($Cl^-$, $NO_3^-$, $SO_4^{2-}$, and $HCO_3^-$) and HA on the degradation of organic contaminants were evaluated. Various buffers with different pH values were employed (details are provided in Text S2). Five reusability tests were performed using the MnCu-5:1 catalyst to examine its cyclability. At the end of each cycle, the catalyst was recovered from the reaction flask, washed several times with deionized water, dried at 80 °C for 12 h, and used in the next cycle.

### 2.5. Sample analysis

The elimination of BPA and other organic contaminants from water was investigated using a high-performance liquid chromatography system equipped with a C18-type column (4.6 × 75 mm, 3.5 μm, Elite 3100, China) and ultraviolet detector ($\lambda$ = 210 nm).

The following mobile phases were used at a flow rate of 1 mL $min^{-1}$: methanol and water (70:30, v/v) for BPA and phenol, and methanol and water (30:70, v/v) for sulfadiazine (SDZ). *p*-Nitrophenol (PNP) was added to 10 mmol of NaOH and detected at $\lambda$ = 400 nm. Methylene blue (MB) and rhodamine B (RhB) were detected at $\lambda$ = 664 and 554 nm, respectively. Details of electrochemical measurements and other analyses can be found in Text S3.

### 2.6. Computational methodology

Density functional theory (DFT) simulations were conducted using the Quantum-ATK software (Version 2019.12). The subsequent data analysis was performed using the VESTA and Virtual NanoLab (Version 2019.12) software programs [29]. The obtained results were used to verify the experimentally observed efficacies of the pristine $Cu_2O$, $Mn_3O_4$, and $Mn_3O_4/Cu_2O$ composite (MnCu) catalysts and PMS interactions. Model structures of $Cu_2O$ and $Mn_3O_4$ were constructed from their unit cells with the space groups of Pn-3m and I4-1/amd, respectively. The $Cu_2O$ lattice parameters were set to a = b = c = 4.25 Å and $\alpha = \beta = \gamma = 90°$, while those for $Mn_3O_4$ were set to a = 11.02 Å, b = c = 5.74 Å, $\alpha = \gamma = 90°$, and $\beta = 121.33°$. The $Mn_3O_4$ unit cell comprised 16 O and 12 Mn atoms, while the $Cu_2O$ unit cell consisted of four Cu and two O atoms within a cubic structure. The optimized unit cell of $Mn_3O_4$ was replicated along a 1 × 2 × 2 grid consisting of 112 atoms with a vacuum space of 10 Å inserted along the c-axis. The unit cell of $Cu_2O$ was replicated along a 2 × 2 × 1 grid followed by a vacuum space of 10 Å. The $Mn_3O_4/Cu_2O$ composite was constructed using 110 atoms with a vacuum space of 10 Å. All these slabs were constructed along the (100) direction based on their

stability. The slab thickness was sufficiently large to ensure that the center of the slab could be considered the bulk phase. A vacuum space of approximately 10 Å was maintained between the slabs to eliminate any fictitious interactions between the periodically repeating slabs.

To investigate the interactions of PMS with $Cu_2O$, $Mn_3O_4$, and the $Mn_3O_4/Cu_2O$ system, a PMS molecule was added to the surface of each slab, and the resulting system was optimized. The relaxed structures of these three species before and after PMS additions are shown in Fig. S1. A linear combination of atomic orbitals was used for Mn, Cu, S, H, and O atoms. The generalized gradient approximation method with the Perdew–Burke–Ernzerhof exchange–correlation functional, Fritz Haber Institute pseudopotentials, and double zeta polarized basis set was employed for structure and energy optimizations. The effective potential, density of states (DOS), electron density difference (EDD), electron density, electrostatic difference potential (ESDP), and electron localization functional (ELF) were computed for the studied systems using the aforementioned method.

## 3. Results and discussion

### 3.1. Characterization of MnCu catalysts

The XRD patterns of the fabricated catalysts are presented in Fig. 1a. The peaks at 2θ = 18.06°, 28.94°, 31.06°, 32.40°, 36.12°, 38.11°, 44,46°, 50.02°, 50.84°, 53.94°, 56.05°, 58.53°, 59.92°, 64.65°, and 74.17° correspond to tetragonal $Mn_3O_4$ with a space group of 14/*m* (PDF #24-0734). The diffraction peaks at 29.59°, 36.46°, 42.33°, 61.36°, and 73.49° indicate the cubic $Cu_2O$ structure (PDF #01-1142). For the MnCu catalysts, all

peaks corresponding to the $Mn_3O_4$ and $Cu_2O$ phases are detected. Fig. 1b shows the Raman spectra of the studied catalysts. Three bands are observed at 300.0, 351.0, and 640.8 $cm^{-1}$, indicating the presence of the $Mn_3O_4$ phase. The strong band at 640 $cm^{-1}$ is attributed to the Mn–O vibrations of divalent manganese ions in the tetrahedral coordination [30,31]. According to previous studies, the two weak bands at 300.0 and 351.0 $cm^{-1}$ can be attributed to the combined vibrations of tetrahedral and octahedral oxygen atoms [30,31]. In addition, four peaks are observed at 139, 213, 405, and 634 $cm^{-1}$, demonstrating the presence of $Cu_2O$ species [32,33]. The intensities of the Raman peaks gradually decrease, and the two weak bands for MnCu-3:1 and MnCu-2:1 at 300.0 and 351.0 $cm^{-1}$ have ultimately disappeared with increasing Cu concentration. The absence of characteristic Cu peaks in the Raman spectra may be due to the effect of Mn on Cu during the growth of the two oxides.

Nanoparticles of various dimensions are detected in the SEM images of the $Mn_3O_4$ and MnCu catalysts (Fig. S2). The average particle sizes of the $Mn_3O_4$, MnCu-10:1, MnCu-5:1, MnCu-3:1, and MnCu-2:1 catalysts are equal to 110, 90, 60, 50, and 47 nm, respectively. Thus, $Mn_3O_4$ nanoparticles are larger than MnCu nanoparticles. The size of MnCu nanoparticles decreases with increasing Cu content, which can be attributed to the growth of the two oxides. The surface morphologies of the catalysts are consistent with those observed via TEM (Fig. 2). Furthermore, MnCu-5:1 nanoparticles exhibit an interplanar spacing of 0.49 nm, indicating the presence of the (101) crystal plane in the $Mn_3O_4$ structure. The interplanar spacing of the (110) crystal planes of $Cu_2O$ nanoparticles is 0.30 nm. According to the particle analysis data, the properties of the

MnCu-5:1 catalyst are consistent with those of the tetragonal $Mn_3O_4$ and cubic $Cu_2O$ phases, confirming their formation in the MnCu-5:1 structure. These results are in good agreement with the XRD patterns (Fig. 1a). The elemental mapping images reveal the presence of Mn, Cu, and O elements in the MnCu-5:1 system; however, they are not uniformly distributed (Figs. 2c–g). Distinct areas enriched in $Cu_2O$ and $Mn_3O_4$ are observed as well. Fig. S3 shows the TEM images of $Mn_3O_4$, MnCu-10:1, MnCu-3:1, and MnCu-2:1, which indicate the formation of $Mn_3O_4$ and $Cu_2O$ species in the MnCu catalysts. Figs. S2(k and l) and S4 display the SEM and TEM images of commercial $Cu_2O$, which exhibit a significantly larger average particle size of 1.5 µm.

The $N_2$ adsorption–desorption isotherms and pore size distribution curves of the $Mn_3O_4$ and MnCu catalysts are shown in Fig. S5. Narrow hysteresis loops are detected for the $Mn_3O_4$, MnCu-10:1, MnCu-5:1, MnCu-3:1, and MnCu-2:1 catalysts in the $P/P_0$ range of 0.8–1.0, indicating the presence of macropores. The BET surface areas of $Mn_3O_4$, $Cu_2O$, MnCu-10:1, MnCu-5:1, MnCu-3:1, and MnCu-2:1 amount to 22.2, 0.61, 34.8, 39.6, 44.9, and 41.9 $m^2\ g^{-1}$, respectively (Table S1). Thus, the surface areas of the catalysts lie in a relatively narrow range, indicating that surface area weakly affects their performance.

### 3.2. Degradation of organic contaminants

The catalytic efficiencies of $Mn_3O_4$, $Cu_2O$, MnCu-10:1, MnCu-5:1, MnCu-3:1, and MnCu-2:1 in the PMS system were evaluated by analyzing the degradation of PNP under the same conditions (Fig. 3). Negligible PNP degradation occurred in the

presence of PMS alone after 30 min at 25 °C (Fig. S6), suggesting that PNP does not degrade in the absence of a catalyst. Among the tested materials, MnCu-5:1 exhibited the highest degradation efficiency (92%) followed by MnCu-3:1 (86%), MnCu-2:1 (82%), MnCu-10:1 (68%), $Cu_2O$ (55%), and $Mn_3O_4$ (10%) after 30 min in the PMS system (Fig. 3a). A physical mixture of $Mn_3O_4$ and $Cu_2O$ in a 5:1 ratio mimicking the metal ratio in MnCu-5:1 was used as a catalyst in a degradation test to verify the synergistic effect. The physical mixture degraded 26% of PNP, which is approximately the average of the values obtained for $Cu_2O$ and $Mn_3O_4$ individually. Therefore, the high performance of MnCu-5:1 likely originated from the synergistic effect between the Mn and Cu oxides within the composite structure rather than simply the combined effect of the individual oxides. The pseudo-first-order kinetic model effectively fitted the PNP degradation curves, which were obtained using various catalysts [34], as shown in Fig. 3b. The corresponding rate constants ($k_1$) are listed in Table S1. MnCu-5:1 exhibits the highest $k_1$ value (0.140 $min^{-1}$), whereas $Mn_3O_4$ and $Cu_2O$ have the $k_1$ values of 0.0063 and 0.041 $min^{-1}$, respectively. Thus, the MnCu-5:1 catalyst demonstrated superior catalytic performance as compared with those of the other catalysts, which can be attributed to its synergistic effect and redox process. After degradation, the reaction solution containing MnCu-5:1 was filtered, and the obtained filtrate was analyzed via inductively coupled plasma–optical emission spectroscopy. The concentrations of $Mn^{2+}$ and $Cu^{2+}$ ions in solution were 0.02 and 0.49 ppm, respectively. Importantly, the provisional recommendation for Cu in drinking water suggested by the World Health Organization is 2 mg/L [35]. Additional tests were performed to confirm the roles of

292 $Mn^{2+}$ and $Cu^{2+}$ ions in the degradation of organic contaminants. The filtered MnCu-5:1
293 solution mediated the degradation of 9% PNP, whereas the $Cu_2O$ solution resulted in
294 the degradation of 41% PNP in the presence of PMS. Notably, the filtered $Mn_3O_4$
295 solution did not exhibit any PNP degradation activity (Fig. S7). These findings highlight
296 the importance of the presence of $Cu^{2+}$ ions for efficient catalysis. The inherent
297 properties of the MnCu-5:1 heterogeneous catalyst strongly influence its performance
298 [5,36]. In the present study, the MnCu-5:1/PMS system efficiently degraded the other
299 tested contaminants. For instance, it degraded 100% of BPA within 10 min, 100% of
300 SDZ and phenol within 15 min, and 95% of MB and RhB within 30 min under the same
301 conditions (Fig. S8). These results demonstrate the potential applicability of the MnCu-
302 5:1/PMS system to various wastewater treatment processes.

303 **3.3. ROS identification**

304 The MnCu-5:1 catalyst activates PMS primarily via radical and nonradical pathways
305 [5,37]. In this work, the contributions of ROS to the reaction were studied by
306 performing quenching experiments using various scavengers to elucidate the activation
307 mechanism of the MnCu-5:1/PMS system. In particular, MeOH, TBA, $CCl_4$, and $CHCl_3$
308 were used to identify radicals in the reaction solution (Fig. 4). MeOH was utilized to
309 identify $SO_4^{\bullet-}$ and •OH radicals, and the corresponding rate constants were $k_{SO4^{\bullet-}} = 2.5$
310 $\times 10^7$ $M^{-1}$ $s^{-1}$ and $k_{\bullet OH} = 9.7 \times 10^8$ $M^{-1}$ $s^{-1}$ [9,38]. The PNP degradation efficiency
311 decreased from 92% to 51% when MeOH (320 mM) was added to the MnCu-5:1/PMS
312 system. After the addition of excess MeOH (640 mM), the PNP degradation efficiency
313 was reduced from 92% to 30%. Further experiments were performed to verify the

presence of radicals in the reaction solution. Methyl phenyl sulfoxide (PMSO) was used as a probe to distinguish between $SO_4^{\bullet-}$ and high-valent metals. PMSO was oxidized to $PMSO_2$ by high-valent metal species, whereas $SO_4^{\bullet-}$ oxidized PMSO and generated hydroxylated and polymeric products [39]. As shown in Figs. S9a–c, minimal $PMSO_2$ formation occurred with and without the MnCu-5:1 catalyst in the PMS system, indicating that SO4•⁻, rather than high-valent metal species, is the primary oxidant for the contaminant degradation process. TBA was used as a scavenger for •OH radicals ($k_{\bullet OH} = 6.0 \times 10^8\ M^{-1}\ s^{-1}$) [40]. The PNP degradation efficiency decreased from 92% to 85% when 320 mM TBA was added to the MnCu-5:1/PMS system. Upon further TBA addition (640 mM), the PNP degradation efficiency was reduced from 92% to 70% under the same conditions. Moreover, the superoxide radical ($O_2^{\bullet-}$) was quenched using $CCl_4$ and $CHCl_3$ [41]; the PNP degradation efficiency decreased slightly when $CCl_4$ (320 mM) and $CHCl_3$ (320 mM) were added separately to the MnCu-5:1/PMS system. These results indicate that radicals, such as $SO_4^{\bullet-}$, •OH, and $O_2^{\bullet-}$, were generated during PNP degradation in the MnCu-5:1/PMS system. Thus, efficient PNP degradation did not occur during the radical scavenging tests, suggesting that PNP was degraded via a radical pathway in the MnCu-5:1/PMS system. In addition, β-carotene dissolved in acetone (2 mL) was used as a scavenger for $^1O_2$ species [42,43]. The β-carotene solution was combined with the PNP solution before PMS, followed by a catalyst addition. When 100 μM of β-carotene was used, the PNP degradation efficiency decreased from 92% to 78% within 30 min in the MnCu-5:1/PMS system (Fig. 4), which indicates a minor contribution of $^1O_2$ toward PNP degradation. From these results, it can be

concluded that the radical pathway is a major pathway for the degradation of organic contaminants in the MnCu-5:1/PMS system. An electron paramagnetic resonance (EPR) technique was used in the subsequent analysis. Experiments were conducted using spin-trapping agents (5,5-dimethylpyrroline N-oxide [DMPO] and 2,2,6,6-tetramethylpiperidine [TEMP]) [43] to demonstrate the contribution of ROS to the degradation process. When MnCu-5:1 was added to the PMS system, no signals corresponding to the DMPO–$SO_4$ and DMPO–OH adducts were observed (Fig. S10a). However, DMPO-X signals with a characteristic 1:1:1 triplet pattern were obtained, indicating the conversion of DMPO to DMPO-X. These results are consistent with those of previous studies that employed the TEMP–$^1O_2$ and EPR techniques [34,44] to investigate the MnCu-5:1/PMS system (Fig. S10b).

### 3.4. $H_2$ temperature-programmed reduction analysis

The $H_2$ temperature-programmed reduction ($H_2$–TPR) profiles of the $Mn_3O_4$, MnCu-10:1, MnCu-5:1, MnCu-3:1, and MnCu-2:1 catalysts were acquired in the 50–800 °C range to examine their redox properties [13], as shown in Fig. S11. The reduction peaks at 201.0, 210.4, 227.2, 262.9, 319.3, 443.0, and 488.0 °C are attributed to MnCu-2:1, MnCu-3:1, MnCu-5:1, MnCu-10:1, CuO, $Cu_2O$, and $Mn_3O_4$, respectively. The structure synthesized in this study (i.e., $Mn_3O_4$–$Cu_2O$) comprised multivalent Mn and Cu species. These results indicate that Mn was present as Mn(III) in $Mn_3O_4$ and reduced to Mn(II), while Cu was present as Cu(I) in $Cu_2O$ and reduced to Cu(0) during the $H_2$–TPR process. In the obtained $H_2$–TPR profile, the peak for MnCu-2:1 was observed at a lower temperature because its Cu content was higher than those of the other catalysts.

This result indicates that the metal species in the catalyst structure underwent the M(III) → M(II)/M(I) →M(0) reduction sequence, which is favorable for the redox cycle of Mn and Cu species in the catalyst.

### 3.5. Electrochemical tests

The different electrochemical performances of the $Mn_3O_4$, $Cu_2O$, MnCu-10:1, MnCu-5:1, MnCu-3:1, and MnCu-2:1 catalysts in the degradation of PNP (Fig. 3) prompted us to investigate their electrochemical properties. The enhanced catalytic activity of the composite catalysts can be ascribed to the efficient redox process between the active metal centers (M(III) ↔ M(II) ↔ M(I)) in the catalyst. To investigate the charge transfer and redox reactions of the catalysts, we conducted cyclic voltammetry (CV), linear sweep voltammetry (LSV), and electrochemical impedance spectroscopy (EIS) measurements. $Mn_3O_4$, $Cu_2O$, MnCu-10:1, MnCu-5:1, MnCu-3:1, and MnCu-2:1 were used as electrodes in a solution containing PMS (0.65 mM) and $Na_2SO_4$ (0.1 M). The obtained CV curves include cathodic and anodic peaks corresponding to the redox reactions of the metal species, which are related to the catalytic reactions occurring on the electrode surfaces [2,28]. Notably, the MnCu-5:1 electrode exhibits stronger oxidation and reduction peaks in the CV curves than those of the $Mn_3O_4$, $Cu_2O$, MnCu-10:1, MnCu-3:1, and MnCu-2:1 electrodes (Figs. 5a and S12). This result demonstrates the crucial role of Cu and Mn species in the catalytic PMS activation, which likely facilitated the rapid electron transfer in the MnCu-5:1 catalyst [28].

The catalysts were also studied using LSV in the 0–2.0 V range (Fig. 5b). MnCu-5:1 exhibits a significantly higher current than those of MnCu-10:1, MnCu-3:1, and MnCu-

2:1, indicating the superior charge-transfer capability of MnCu-5:1 as compared with those of other catalysts owing to the strong interactions between Cu and Mn species in the catalyst structure. The easily oxidizable metal species contributed to the superior catalytic performance of MnCu-5:1 in PMS activation. The EIS Nyquist plots (Fig. 5c) reveal a lower charge-transfer resistance of MnCu-5:1 as compared with those of $Mn_3O_4$ and $Cu_2O$. These observations indicate that MnCu-5:1 exhibited a higher electrical conductivity than those of the other catalysts, facilitating the efficient and rapid electron transfer to PMS.

Open-circuit potential (OCP) measurements were conducted to provide insights into the electron-transfer mechanism. The obtained OCP curve (Fig. 5d) characterizes the behavior of the MnCu-5:1 electrode in a $Na_2SO_4$ (0.5 M) solution. PMS (0.64 mM) was added to this solution during the experiment. The efficient redistribution of electron density was achieved when MnCu-5:1 was deposited on the working electrode and PMS was physisorbed on the catalyst surface [2,45]. The MnCu-5:1–PMS complex was formed under these conditions [45]. A large positive increase in potential from 0.210 to 0.950 V was observed when the MnCu-5:1 electrode was used with PMS. When $Cu_2O$ and $Mn_3O_4$ were used with PMS, the potential increased from 0.115 to 0.7809 V and 0.153 to 0.462 V, respectively, indicating changes in the electron distribution. These results suggest that the MnCu-5:1 catalyst with a synergistic effect strongly interacted with PMS. Under these conditions, efficient electron transfer and complex formation occurred between the catalyst surface and PMS. Next, PMS decomposition experiments with and without PNP were performed using the MnCu-5:1 catalyst (Fig. 6a).

Approximately 100% of PMS was degraded within 25 min over the MnCu-5:1 catalyst without PNP; in contrast, a negligible amount of PMS degraded in the presence of PNP without a catalyst. In the presence of both PNP and MnCu-5:1, 96% of PMS degraded within 30 min. These results indicate that PMS decomposition occurred on the catalyst surface, while PNP degraded in the presence of the catalyst/PMS system via a radical pathway, suggesting that PMS and the catalyst interact to generate radicals for PNP degradation. Furthermore, MnCu-5:1 exhibited the highest PMS degradation efficiency among the tested catalysts (Fig. 6b), confirming the existence of synergistic effects in the MnCu-5:1 structure, making it a superior catalyst for PMS activation.

The surface compositions of $Mn_3O_4$ and the MnCu composite catalysts were determined via XPS (Figs. 7a–f and S13–S16). XPS peak fitting was conducted before and after the catalytic reaction. The Mn $2p_{3/2}$ peak was deconvoluted into three peaks at 640.6 ± 0.3, 642.0 ± 0.2, and 644.0 ± 0.5 eV, corresponding to Mn(II), Mn(III), and Mn(IV) species [13,17], respectively (Figs. 7a, 7d, and S14). After degradation, the area of the Mn(II) peak decreased from 31.7% to 12.6%, and that of the Mn(IV) peak decreased from 28.8% to 21.2%. In contrast, the peak area of the Mn(III) peak increased from 39.5% to 66.2% (Figs. 7a and d), indicating a change in the oxidation state of the surface Mn species.

XPS peak fitting was also performed for the Cu peaks before and after the catalytic reaction. The Cu $2p_{3/2}$ peak was deconvoluted into three peaks at 931.0 ± 0.3, 933.8 ± 0.2, and 935.0 ± 0.2 eV, corresponding to Cu(I), Cu(II)–O, and Cu(II)–OH, respectively [24] (Figs. 7b, 7e, and S15). After the catalytic reaction, the areas of the Cu(I) and

Cu(II)–O peaks decreased from 10.8% to 7.1% and 65.4% to 60.6%, respectively, whereas that of the Cu(II)–OH peak increased from 23.8% to 32.3% (Figs. 7b and e). These results indicate that PMS oxidized low-valent metal species to generate radicals that subsequently degraded PNP. Thus, the XPS data confirm the observed changes in the Mn and Cu oxidation states, indicating their involvement in PMS activation. These results indicate that electron transfer easily occurs within the surface-complexed MnCu-5:1/PMS system, potentially enhancing the radical generation process. The O 1s spectra of the $Mn_3O_4$ and MnCu catalysts are presented in Figs. 7c, 7f, and S16. Their deconvolution produced three peaks at 529.8 ± 0.2 (O(I)), 531.3 ± 0.3 (O(II)), and 533.1 ± 0.5 (O(III)) eV, corresponding to the lattice oxygen, –OH, and adsorbed $H_2O$ species, respectively [28]. After the reaction completion, the areas of the lattice oxygen peaks decreased from 60.4% to 54.0%, while those of the –OH and adsorbed $H_2O$ peaks increased from 35.1% to 40.1% and 5.5% to 5.9%, respectively (Figs. 7c and f). This phenomenon can be attributed to the reduction of the higher-valent Cu and Mn atoms to the lower-valent states during the decomposition of $\equiv Mn^{(III/IV)}–O–Cu^{(II/III)}—OSO_3—$ OH species. These results indicate that O species contributed to the catalytic reaction and participated in the PMS activation pathway [28,34]. The –OH species on the catalyst surface provide active sites for the bond formation with PMS [5,34]. The MnCu-5:1 surface has a higher content of –OH species (35.1%) than those of the $Mn_3O_4$ (25.1%), MnCu-10:1 (32.6%), MnCu-3:1 (31.7%), and MnCu-2:1 (33.4%) surfaces, as shown in Figs. 7c, 7f, and Fig. S16.

According to the DFT-simulated EDD values, $Mn_3O_4$ likely withdraws electrons from

$Cu_2O$ within the $Mn_3O_4$–$Cu_2O$ composite, increasing the positive charge of $Cu_2O$ species. This can induce the transformations of Mn(III) to Mn(II) and Cu(I) to Cu(II). Upon the interaction with PMS ($HSO_5^-$), the most active sites in the composite structure are $Cu_2O$ species ($Mn_3O_4$–$Cu_2O$), which become more positive. Therefore, the PMS interaction with the $Mn_3O_4$–$Cu_2O$ composite renders the $Cu_2O$ region more negatively charged, whereas the $Mn_3O_4$ sites of the $Mn_3O_4$–$Cu_2O$ composite become positively charged. As a result, the Cu oxidation state changes from Cu(II) to Cu(I), while Mn(II) is transformed to Mn(III). A plausible mechanism for the activation of PMS by the MnCu-5:1 catalyst is illustrated in Scheme 1. First, the physisorption of $H_2O$ molecules on the catalyst surface generates –OH species. Next, the Mn(II/III)–$OSO_3$ complex is formed via the reaction between Mn(II/III)–OH and $HSO_5^-$ [46]. Subsequently, $HSO_5^-$ can accept an electron from Mn(II)/Mn(III) to produce Mn(III)/Mn(IV), leading to the formation of the $SO_4^{\bullet-}$ radical after the cleavage of the O–O bond in the $HSO_5^-$ according to Eqs. (1–3).

Previous studies have revealed that Cu(I) in Cu-based bimetallic oxide catalysts is oxidized to Cu(II) by $HSO_5^-$ [23–25]. In the present work, considering that Cu existed as $Cu_2O$ in MnCu, Cu(I) in $Cu_2O$ likely underwent oxidation by PMS, forming Cu(II) and $SO_4^{\bullet-}$ species. Furthermore, PMS can activate Cu(II), generating the Cu(II)–$(HO)OSO_3^-$ complex and transferring one electron to this complex to promote the further oxidation of Cu(II) to Cu(III), thereby generating another $SO_4^{\bullet-}$ radical [46]. The formation of Cu(III) during the reaction of MnCu-5:1 with PMS was also supported by $NaIO_4$ test results. When $NaIO_4$ was added to trap Cu(III) as a stable Cu(III)−$IO_4$

complex, a characteristic absorption peak was observed at 420 nm. As shown in Figs. S17a–c, this peak confirms the generation of Cu(III) species in the MnCu-5:1/PMS (Fig. S17a) and $Cu_2O$/PMS (Fig. S17b) systems. Notably, the peak intensity of the Cu(III)−$IO_4^-$ complex increased with increasing reaction time, indicating continuous Cu(III) formation. Importantly, the MnCu-5:1 catalyst generated Cu(III) at a higher concentration than that obtained for $Cu_2O$ during PMS activation. In addition, PMS can reduce the formed Cu(II) species to produce $SO_5^{\bullet-}$ radicals. Therefore, the redox cycle involving various Cu oxidation states (Cu(I) ↔ Cu(II) ↔ Cu(III)) plays a significant role in the PMS activation process (Eqs. (1–3)). The generated $SO_5^{\bullet-}$ radicals reacted with PMS to produce $^1O_2$ species (Eq. (4)) or with $OH^-/H_2O$ to form •OH radicals (Eq. (5)).

$$\equiv Mn^{(II/III)}–O–Cu^{(I/II)}–OH^- + HSO_5^- \rightarrow \equiv Mn^{(II/III)}–O–Cu^{(I/II)}—OSO_3—OH + OH^- \quad (1)$$

$$\equiv Mn^{(II/III)}–O–Cu^{(I/II)}—OSO_3—OH \rightarrow \equiv Mn^{(III/IV)}–O–Cu^{(II/III)}–OH^- + SO_4^{\bullet-} \quad (2)$$

$$\equiv Mn^{(III/IV)}–O–Cu^{(II/III)}—OSO_3—OH + H_2O \rightarrow \equiv Mn^{(II/III)}–O–Cu^{(I/II)}–OH + SO_5^{\bullet-} + H^+ \quad (3)$$

$$SO_5^{\bullet-} + {}^-OSO_3—OH \rightarrow SO_4^{2-} + {}^1O_2 + HSO_4^- \quad (4)$$

$$SO_4^{\bullet-} + H_2O/OH^- \rightarrow SO_4^{2-} + \bullet OH \quad (5)$$

### 3.6. DFT calculations

To validate our experimental data, we performed DFT studies using the two-dimensional $Cu_2O$, $Mn_3O_4$, and $Mn_3O_4$–$Cu_2O$ slab models. Based on their interactions with PMS, the catalytic efficiencies of these models were predicted in terms of their PMS adsorption energies. The adsorption energies of PMS on the pristine $Cu_2O$, $Mn_3O_4$,

and $Mn_3O_4$–$Cu_2O$ composite surfaces were calculated using Eq. (6), and the obtained values are listed in Table S2.

$$\Delta E_{ad} = E_{surface@PMS} - (E_{PMS} + E_{surface}), \quad (6)$$

where $\Delta E_{ad}$ is the adsorption energy, $E_{surface}$ is the energy of the pristine surface, $E_{PMS}$ is the total free energy of PMS, and $E_{surface@PMS}$ is the energy of the optimized PMS–slab complex. According to Figs. S1d–f, the oxygen atoms of PMS interact with the surface Mn or Cu atoms of $Cu_2O$, $Mn_3O_4$, and the $Mn_3O_4$–$Cu_2O$ composite. These interactions are observed in the ELF maps presented in Figs. 8b, 8d, and 8f. In this context, the interaction energies of PMS with the pristine $Cu_2O$ and $Mn_3O_4$ surfaces were −5.76 and −4.85 eV, respectively. However, for the $Mn_3O_4$–$Cu_2O$ composite, the PMS adsorption energy increased to −7.21 eV (Table S2). As shown in Fig. 8f, PMS shared its electronic cloud density with the $Mn_3O_4$–$Cu_2O$ composite, resulting in strong electrostatic bonding. This phenomenon indicates that the $Mn_3O_4$–$Cu_2O$ composite exhibited a higher reactivity towards PMS, as confirmed by its high adsorption energy of −7.21 eV. These results strongly corroborate the experimental data and confirm that the $Mn_3O_4$–$Cu_2O$ composite remarkably improves the catalytic efficiency of the PMS system.

It is well known that $Cu_2O$ and $Mn_3O_4$ are semiconductors with bandgaps, as shown in Figs. S18 and S19. The DOS plots of the $Cu_2O$, $Mn_3O_4$, and $Mn_3O_4$–$Cu_2O$ surfaces (Fig. 9) contain zero bandgaps, suggesting the presence of potential surface states and dangling bonds and that PMS strongly interacted with all three species. However, a noticeable enhancement is observed in the DOS plot of the composite near the Fermi

512 energy (from 0 to −2 eV) as compared with those of $Cu_2O$ and $Mn_3O_4$, which confirms
513 the existence of strong interactions between PMS and the $Mn_3O_4$–$Cu_2O$ composite.
514 Notably, the enhanced interactions between PMS and the $Mn_3O_4$–$Cu_2O$ composite can
515 potentially improve its catalytic performance in various applications. The high
516 adsorption energy indicates a strong affinity between the catalyst and PMS, which can
517 increase the efficiency of catalytic reactions. Moreover, the DOS shift near the Fermi
518 energy may influence the electronic properties of the composite, potentially opening
519 new avenues for its use in electronic devices.
520 To elucidate the remarkably enhanced performance of the composite catalyst as
521 compared with those of pristine $Cu_2O$ and $Mn_3O_4$, we conducted ESDP simulations for
522 all three catalysts with and without PMS interactions (Fig. 10). According to Figs. 10a–
523 c, the ESDP noticeably shifted from its original position upon the catalyst interaction
524 with PMS, indicating the high catalytic capabilities of these species.
525 However, Fig. 10c reveals that charge transfer occurs within the composite, which
526 enhances its catalytic activity. Fig. 10c clearly shows both the $Cu_2O$ and $Mn_3O_4$ sites of
527 the composite structure. The ESDP of $Mn_3O_4$ in the composite became negatively
528 charged with respect to that of pristine $Mn_3O_4$, while $Cu_2O$ donated this charge and
529 became positively charged. This charge redistribution within the composite not only
530 enhances its catalytic performance but also alters its electronic properties, influencing
531 its potential applications. For instance, the negative charge at the $Mn_3O_4$ site can
532 increase its reactivity towards positively charged species, while the positive charge at
533 the $Cu_2O$ site attracts negatively charged species, which broadens the range of catalytic

reactions for this composite.

The enhanced catalytic activity of the $Mn_3O_4$–$Cu_2O$ composite due to its strong interaction with PMS was confirmed by the results of EDD simulations. The comparative EDD plots constructed for pristine $Cu_2O$, $Mn_3O_4$, and $Mn_3O_4$–$Cu_2O$ with and without PMS interactions are displayed in Fig. S20. In this figure, the areas highlighted in yellow and green represent the negative and positive potentials at the catalyst/PMS interface, respectively. For the $Mn_3O_4$–$Cu_2O$/PMS system, the interactions between PMS and $Mn_3O_4$–$Cu_2O$ are driven by strong electrostatic forces, leading to a significant charge transfer between these two components (Fig. S20c). This substantial inter-charge exchange is not confined to the interface but is extended throughout the bulk of the $Mn_3O_4$–$Cu_2O$/PMS system, thus increasing its catalytic ability.

This significant charge transfer can have several implications, such as increasing the composite reactivity toward PMS. Additionally, the charge redistribution may alter the electronic structure of the composite (Fig. 9) (*vide supra*), potentially influencing its electrical and optical properties.

We also simulated the effective potential maps of the three catalysts (Fig. S21). A comparative analysis revealed that the effective potential of the $Cu_2O$ bulk region ranged between −0.1 and −0.7 eV, while that of $Mn_3O_4$ varied between −0.5 and −1.0 eV (Figs. S21a and S21b, respectively). Conversely, the effective potential of the $Mn_3O_4$–$Cu_2O$ composite was more optimal as compared with those of pristine $Cu_2O$ and $Mn_3O_4$, ranging between −0.3 and −0.8 eV, which is consistent with the discussion

556 on the EDD and charge transformation results.

557 The optimal effective potential of the $Mn_3O_4$–$Cu_2O$ composite, which is a measure of
558 electrostatic interactions between a test charge and the system, can contribute to its
559 enhanced catalytic performance. Therefore, the optimal effective potential indicates a
560 more favorable electrostatic environment for catalysis, which can increase the
561 efficiency of catalytic reactions and potentially broaden the range of reactions catalyzed
562 by the composite.

563 **3.7. Influence of reaction parameters on PNP degradation efficiency**

564 **3.7.1. Effects of MnCu-5:1 and PMS content on the extent of PNP degradation**

565 Figs. S22a and b show the influences of the MnCu-5:1 and PMS contents on the
566 degradation of PNP. When 0.05 g $L^{-1}$ of MnCu-5:1 was used, 92% of PNP was
567 degraded within 30 min, whereas 0.2, 0.4, and 0.8 g $L^{-1}$ of MnCu-5:1 degraded 92% of
568 PNP within 25, 15, and 10 min, respectively (Fig. S22a). These results indicate that the
569 PNP degradation efficiency increased in the presence of PMS owing to the increase in
570 the number of active sites with increasing MnCu-5:1 content [5]. Fig. S20b shows the
571 influence of the PMS content on the PNP degradation process in the presence of MnCu-
572 5:1. When the PMS content increased from 0.16 to 0.65 mM, the PNP degradation
573 efficiency increased from 15% to 92% within 30 min. Increasing the PMS concentration
574 to 1.3 and 2.6 mM resulted in the complete degradation of PNP within 10 and 2.5 min,
575 respectively, which indicates that excess PMS enhanced the catalytic activity of MnCu-
576 5:1, promoting PNP degradation [5].

577 **3.7.2. Effect of initial pH on PNP degradation efficiency**

The initial pH of the reaction solution plays a crucial role in degrading organic contaminants in water bodies. To investigate the influence of the solution pH on PNP degradation under the same reaction conditions, degradation experiments were performed using the MnCu-5:1/PMS system at initial pH values of 3.5, 5.5, 7.5, 8.2, 9.5, and 10.5. At pH values of 5.5, 7.5, 8.2, and 9.5, 70%, 85%, 92%, and 74% of PNP were degraded (Fig. S22c), whereas at pH values of 3.5 and 10.5, 37% and 7% of PNP were degraded, respectively. Therefore, the PNP degradation efficiency gradually decreased as the initial solution pH increased from 8.2 to 10.5. In addition, the PNP degradation efficiency decreased with decreasing pH from 5.5 to 3.5. Thus, the PNP degradation efficiency over the MnCu-5:1/PMS system was significant at neutral pH and decreased under the highly basic and acidic pH conditions. Under the basic pH conditions, the interactions between MnCu-5:1, PMS, and PNP weakened because of the increased electrostatic repulsion force. The pKa of PNP was 7.15 [47], whereas that of PMS ($HSO_5^-$) was 9.4 [27]. PNP was deprotonated at pH = 10.5, yielding negatively charged PNP units. Therefore, the interactions between MnCu-5:1 and PNP became weaker, thereby decreasing the PNP degradation efficiency. Under the highly acidic pH conditions, PNP degradation may be affected by the availability of active sites on the catalyst surface and substantial leaching of Cu and Mn ions from the catalyst into the solution.

### 3.7.3. Influence of anions and HA on PNP degradation efficiency

Most inorganic anions can act as scavengers and suppress contaminant degradation via radical pathways. Hence, the influences of various anions (5 mM), such as $SO_4^{2-}$, $Cl^-$,

600 $NO_3^-$, $HCO_3^-$, and HA, on PNP degradation were studied using the MnCu-5:1/PMS
601 system (Fig. S22d). $SO_4^{2-}$, $Cl^-$, and $NO_3^-$ exhibited negligible inhibitory effects on PNP
602 degradation [8]. $Cl^-$ and $NO_3^-$ ions commonly exist in water bodies and can react with
603 $SO_4$•$^-$ and •OH radicals to generate Cl•$^-$ and $NO_3$•$^-$ species. When 5 mM of $HCO_3^-$ was
604 added to the reaction system, the PNP degradation efficiency decreased from 92% to
605 78%. The common free radical scavenger $HCO_3^-$ may react quickly with $SO_4$•$^-$ and
606 HO· to form $CO_3$•$^-$ [3,48]. The generated radicals possess poor oxidation properties,
607 which decrease the contaminant degradation rate [8,48]. This demonstrates that $SO_4$•$^-$
608 species were involved in the degradation of contaminants and that the studied anions
609 caused slight PNP degradation. To investigate the effect of organic matter, we examined
610 the influence of HA on PNP degradation in the MnCu-5:1/PMS system. The PNP
611 degradation efficiency decreased from 92% to 80% in the presence of 5 mg $L^{-1}$ HA
612 (Fig. S22d). This effect can be attributed to the occurrence of reactions between radicals
613 and organic matter or competitive reactions between MnCu-5:1/PMS, PNP, and organic
614 matter [5].

615 **3.8. Cycling tests and MnCu-5:1 stability**

616 Stability and cyclability are important characteristics of an effective heterogeneous
617 catalytic system. In this study, five consecutive cycling tests were performed to evaluate
618 the cyclability of MnCu-5:1 during PNP degradation. The PNP degradation efficiency
619 slightly increased during the subsequent cycles (Fig. S23a), indicating that the MnCu-
620 5:1 catalyst exhibits high cycling performance. PMS can be easily activated in the
621 presence of multivalent Mn/Cu and low-valent Cu species. The slightly increased

622 catalytic activity may be caused by the increased number of surface –OH groups (Fig.
623 7f). The crystal structure of MnCu-5:1 was also investigated. Notably, the peak
624 positions in the obtained XRD pattern remained unchanged after oxidation (Fig. S23b),
625 indicating that the MnCu-5:1 crystal structure was stable. The SEM images of the used
626 MnCu-5:1 catalyst show that its surface morphology is similar to that of the fresh
627 catalyst (Figs. S23c and d). Hence, the catalyst surface morphology and crystal structure
628 remained unchanged during the cycling tests. These results indicate that MnCu-5:1
629 exhibits good cyclability and stability during PNP degradation in the presence of PMS.

630 **3.9. Plausible degradation pathway**

631 To identify the intermediate products generated during PNP degradation and propose
632 plausible degradation pathways, the products formed during PNP degradation in the
633 MnCu-5:1/PMS system were analyzed via liquid chromatography–mass spectrometry.
634 Nine major intermediate degradation products (P1–P9) were detected ($m/z$ = 187, 183,
635 169, 123, 110, 109, 113, 73, and 71, respectively) (Fig. S24). Structural formulas for
636 these products were proposed based on the fragmentation data provided in Table S3.
637 The presence of small molecules in the degraded solution indicates efficient PNP
638 degradation in the MnCu-5:1/PMS system. The proposed PNP degradation is shown in
639 Fig. S25, which is consistent with the results of previous works [49,50]. Initially, ROS
640 attacked PNP, leading to the cleavage of the nitro/hydroxyl group within the phenol
641 ring, which resulted in the degradation of PNP into aromatic ring compounds. The
642 aromatic ring was broken into smaller products, including butanal, propionic acid, and
643 4-heptanone, via an oxidative ring-opening reaction. Subsequently, these acidic

644 products were directly degraded into $CO_2$ and $H_2O$. Furthermore, the bioaccumulation
645 potential of the intermediate product P8 was significantly reduced. However, an
646 analysis conducted using toxicity estimation software (version 5.1) revealed that most
647 intermediate products (P1–P9) were more toxic than PNP (Table S3), indicating that
648 the toxicity of most intermediate products decreased. In addition, a total organic carbon
649 analysis showed a 44% reduction degree within 30 min after 50 mM PNP was added to
650 the MnCu-5:1/PMS system. These results suggest that the MnCu-5:1/PMS system
651 effectively degraded PNP and promoted its mineralization during wastewater treatment.

652 **4. Conclusions**

653 In this study, a highly efficient MnCu-5:1 catalyst based on bimetallic $Mn_3O_4$–$Cu_2O$
654 oxides was developed for degrading organic pollutants. Among the tested MnCu
655 composites, MnCu-5:1 exhibited superior performance owing to the synergistic effect
656 between Mn and Cu, efficient electron transfer, and high concentration of –OH groups
657 on the catalyst surface. The results of scavenging experiments demonstrated that the
658 MnCu-5:1 catalyst effectively degraded contaminants via a radical pathway.
659 Computational modeling data revealed a significant increase in the PMS adsorption
660 energy on the MnCu-5:1 composite surface as compared with those of $Mn_3O_4$ and
661 $Cu_2O$, which is attributed to the electron transfer from $Cu_2O$ to $Mn_3O_4$, rendering $Cu_2O$
662 more positively charged and $Mn_3O_4$ more nucleophilic. This charge distribution
663 optimized the overall electronic properties of the composite. Notably, a strong
664 correlation was observed between the adsorption energy and catalytic activity,
665 indicating that stronger adsorption increases the PNP degradation efficiency. The

MnCu-5:1/PMS system effectively degraded PNP between the neutral and slightly basic pH values (5.5–9.0). The presence of common anions and HA weakly affected the PNP degradation efficiency. These findings highlight the effectiveness of the MnCu-5:1 catalyst owing to its synergistic effect and unique catalytic properties, and PMS activation proceeded via the radical and minor nonradical pathways. Additionally, the fabricated catalysts exhibited low environmental toxicity, making them promising candidates for developing green and sustainable wastewater treatment methods.

## Acknowledgments

The authors are grateful for the funding provided by the National Natural Science Foundation of China (51978542) and Young Foreign Talent Program of Ministry of Science and Technology of China (QN2022027001).

## References

[1] S. Liu, C. Lai, B. Li, C. Zhang, M. Zhang, D. Huang, L. Qin, H. Yi, X. Liu, F. Huang, X. Zhou, L. Chen, Role of radical and non-radical pathway in activating persulfate for degradation of p-nitrophenol by sulfur-doped ordered mesoporous carbon, Chemical Engineering Journal 384 (2020). https://doi.org/10.1016/j.cej.2019.123304.

[2] A. Khan, H. Ullah, Q. Wu, W. Gong, L. Ma, S. Zhao, A. Xu, X. Li, Efficient degradation of organic contaminants in aqueous media using oxygen vacancy-rich MnO catalyst via peroxymonosulfate activation, Chemical Engineering Journal 472 (2023). https://doi.org/10.1016/j.cej.2023.145112.

[3] J. Iqbal, N.S. Shah, J. Ali Khan, Mu. Naushad, G. Boczkaj, F. Jamil, S. Khan, L. Li, B. Murtaza, C. Han, Pharmaceuticals wastewater treatment via different advanced oxidation processes: Reaction mechanism, operational factors, toxicities, and cost evaluation – A review, Sep Purif Technol 347 (2024) 127458. https://doi.org/10.1016/j.seppur.2024.127458.

[4] H. Chen, X. Li, W. Li, J. Feng, Y. Zhao, H. Zhang, Y. Ren, Nitrogen-doped biochar/MnO2 as an efficient PMS activator for synergistic BPA degradation via non-free radical pathways in the water, J Environ Chem Eng 12 (2024). https://doi.org/10.1016/j.jece.2024.112446.

[5] A. Khan, K. Zhang, A. Taraqqi-A-Kamal, X. Wang, Y. Chen, Y. Zhang, Degradation of antibiotics in aqueous media using manganese nanocatalyst-activated peroxymonosulfate, J Colloid Interface Sci 599 (2021). https://doi.org/10.1016/j.jcis.2021.04.095.

[6] F. Wang, Y.H. Li, Y. Gao, Y. Chai, Y. Wei, C.C. Wang, P. Wang, H. Fu, C. Zhao, Ultrafast removal of organics via peroxymonosulfate activation over Co2P/TD hollow spheres derived from

ZIF-67, Chemical Communications 60 (2024). https://doi.org/10.1039/d4cc00280f.
[7] Y. Jiang, X. Weng, Y. Hu, Y. Lv, Z. Yu, Y. Liu, X. Li, C. Lin, X. Ye, G. Yang, M. Liu, Enhanced peroxymonosulfate (PMS) activation process mediated by vanadium modified CoO catalyst for rapid degradation of organic pollutants: Insights into the role of V, J Environ Chem Eng 12 (2024). https://doi.org/10.1016/j.jece.2024.111941.
[8] Y. Han, C. Zhao, W. Zhang, Z. Liu, Z. Li, F. Han, M. Zhang, F. Xu, W. Zhou, Cu-doped CoOOH activates peroxymonosulfate to generate high-valent cobalt-oxo species to degrade organic pollutants in saline environments, Appl Catal B 340 (2024). https://doi.org/10.1016/j.apcatb.2023.123224.
[9] A. Khan, Z. Liao, Y. Liu, A. Jawad, J. Ifthikar, Z. Chen, Synergistic degradation of phenols using peroxymonosulfate activated by CuO-Co3O4@MnO2 nanocatalyst, J Hazard Mater 329 (2017). https://doi.org/10.1016/j.jhazmat.2017.01.029.
[10] K.-X. Li, F.-X. Wang, Z.-C. Zhang, Z.-X. Liu, Y.-H. Ma, C.-C. Wang, P. Wang, Peroxymonosulfate activation over amorphous ZIF-62(Co) glass for micropollutant degradation, Chinese Journal of Catalysis 59 (2024) 118–125. https://doi.org/10.1016/S1872-2067(23)64608-X.
[11] J. Du, J. Bao, Y. Liu, S.H. Kim, D.D. Dionysiou, Facile preparation of porous Mn/Fe3O4 cubes as peroxymonosulfate activating catalyst for effective bisphenol A degradation, Chemical Engineering Journal 376 (2019). https://doi.org/10.1016/j.cej.2018.05.177.
[12] J.C.E. Yang, Y. Lin, H.H. Peng, B. Yuan, D.D. Dionysiou, X.D. Huang, D.D. Zhang, M.L. Fu, Novel magnetic rod-like Mn-Fe oxycarbide toward peroxymonosulfate activation for efficient oxidation of butyl paraben: Radical oxidation versus singlet oxygenation, Appl Catal B 268 (2020). https://doi.org/10.1016/j.apcatb.2019.118549.
[13] F. Wang, M. Xiao, X. Ma, S. Wu, M. Ge, X. Yu, Insights into the transformations of Mn species for peroxymonosulfate activation by tuning the Mn3O4 shapes, Chemical Engineering Journal 404 (2021). https://doi.org/10.1016/j.cej.2020.127097.
[14] Z. Wang, Y. Ma, H. Lin, L. Luo, H. Zhang, Zn-Mn bimetallic oxide derived from waste battery to activate peroxymonosulfate for bisphenol A removal under visible light irradiation, J Environ Chem Eng 12 (2024) 113351. https://doi.org/10.1016/j.jece.2024.113351.
[15] X. Zhou, S. Shen, P. Wang, X. Wei, R. Zhang, H. Tang, H. Wang, W. Lu, J. Wang, Research progress on catalytic activation of peroxymonosulfate based on manganese oxides, J Environ Chem Eng 10 (2022). https://doi.org/10.1016/j.jece.2022.108937.
[16] Q. Wang, S. Liu, J. Lu, Facile synthesis of three-dimensional MnOX (MnO2, Mn2O3, Mn3O4) hierarchical microflower for removal of phenol through peroxymonosulfate activation, Mater Lett 358 (2024). https://doi.org/10.1016/j.matlet.2023.135807.
[17] A. Khan, S. Zou, T. Wang, J. Ifthikar, A. Jawad, Z. Liao, A. Shahzad, A. Ngambia, Z. Chen, Facile synthesis of yolk shell Mn2O3@Mn5O8 as an effective catalyst for peroxymonosulfate activation, Physical Chemistry Chemical Physics 20 (2018). https://doi.org/10.1039/c8cp02080a.
[18] Y.-C. Zhang, S. Ullah, R. Zhang, L. Pan, X. Zhang, J.-J. Zou, Manipulating electronic delocalization of Mn3O4 by manganese defects for oxygen reduction reaction, Appl Catal B 277 (2020) 119247. https://doi.org/10.1016/j.apcatb.2020.119247.
[19] Q. Wang, Y. Li, Z. Shen, X. Liu, C. Jiang, Facile synthesis of three-dimensional Mn3O4 hierarchical microstructures for efficient catalytic phenol oxidation with peroxymonosulfate, Appl Surf Sci 495 (2019).

https://doi.org/10.1016/j.apsusc.2019.143568.
[20] L. Wang, N. Jiang, H. Xu, Y. Luo, T. Zhang, Trace Cu(II)-Mediated Selective Oxidation of Benzothiazole: The Predominance of Sequential Cu(II)-Cu(I)-Cu(III) Valence Transition and Dissolved Oxygen, Environ Sci Technol 57 (2023). https://doi.org/10.1021/acs.est.3c04134.
[21] P. Yan, J. Shen, S. Wang, Y. Zhou, J. Kang, L. Yuan, L. Bi, Y. Li, Z. Chen, Removal of 2,6-dichlorophenol in water by CuO activated peroxymonosulfate: Efficiency, mechanism and degradation pathway, Sep Purif Technol 254 (2021). https://doi.org/10.1016/j.seppur.2020.117630.
[22] H. Li, J. Tian, F. Xiao, R. Huang, S. Gao, F. Cui, S. Wang, X. Duan, Structure-dependent catalysis of cuprous oxides in peroxymonosulfate activation via nonradical pathway with a high oxidation capacity, J Hazard Mater 385 (2020). https://doi.org/10.1016/j.jhazmat.2019.121518.
[23] C. Yin, S. Zhou, K. Zhang, J. Bai, Y. Lv, X. Zhang, X. Li, A. Xu, Crednerite CuMnO2 as highly efficient Fenton-like catalysts for p-nitrophenol removal:Synergism between Cu(I) and Mn (III), J Clean Prod 319 (2021). https://doi.org/10.1016/j.jclepro.2021.128640.
[24] C. Yin, A. Khan, Q. Gao, Q. Li, X. Zhou, X. Liu, A. Xu, X. Li, Synergistic activation of peroxymonosulfate for efficient aqueous p-nitrophenol degradation with Cu(II) and Ag(I) in Ag2Cu2O3, Sep Purif Technol 291 (2022). https://doi.org/10.1016/j.seppur.2022.120934.
[25] Y. Feng, D. Wu, Y. Deng, T. Zhang, K. Shih, Sulfate Radical-Mediated Degradation of Sulfadiazine by $CuFeO_2$ Rhombohedral Crystal-Catalyzed Peroxymonosulfate: Synergistic Effects and Mechanisms, Environ Sci Technol 50 (2016) 3119–3127. https://doi.org/10.1021/acs.est.5b05974.
[26] Y. Feng, J. Liu, D. Wu, Z. Zhou, Y. Deng, T. Zhang, K. Shih, Efficient degradation of sulfamethazine with CuCo2O4 spinel nanocatalysts for peroxymonosulfate activation, Chemical Engineering Journal 280 (2015). https://doi.org/10.1016/j.cej.2015.05.121.
[27] X. Liu, J. Zhou, Q. Xia, B. Li, Q. Gao, S. Zhao, A. Khan, A. Xu, X. Li, Modified birnessite MnO2 as efficient Fenton-like catalysts through electron transfer process between the simultaneously surface-activated peroxymonosulfate and pollutants, J Hazard Mater 443 (2023). https://doi.org/10.1016/j.jhazmat.2022.130178.
[28] Z. Dong, Q. Zhang, B.Y. Chen, J. Hong, Oxidation of bisphenol A by persulfate via Fe3O4-A-MnO2 nanoflower-like catalyst: Mechanism and efficiency, Chemical Engineering Journal 357 (2019). https://doi.org/10.1016/j.cej.2018.09.179.
[29] S. Smidstrup, T. Markussen, P. Vancraeyveld, J. Wellendorff, J. Schneider, T. Gunst, B. Verstichel, D. Stradi, P.A. Khomyakov, U.G. Vej-Hansen, M.E. Lee, S.T. Chill, F. Rasmussen, G. Penazzi, F. Corsetti, A. Ojanperä, K. Jensen, M.L.N. Palsgaard, U. Martinez, A. Blom, M. Brandbyge, K. Stokbro, QuantumATK: An integrated platform of electronic and atomic-scale modelling tools, Journal of Physics Condensed Matter 32 (2020). https://doi.org/10.1088/1361-648X/ab4007.
[30] D. Lan, M. Qin, R. Yang, H. Wu, Z. Jia, K. Kou, G. Wu, Y. Fan, Q. Fu, F. Zhang, Synthesis, characterization and microwave transparent properties of Mn3O4 microspheres, Journal of Materials Science: Materials in Electronics 30 (2019) 8771–8776. https://doi.org/10.1007/s10854-019-01201-7.
[31] H.U. Shah, F. Wang, A.M. Toufiq, S. Ali, Z.U.H. Khan, Y. Li, J. Hu, K. He, Electrochemical Properties of Controlled Size $Mn_3O_4$ Nanoparticles for Supercapacitor Applications, J

Nanosci Nanotechnol 18 (2018) 719–724. https://doi.org/10.1166/jnn.2018.14644.
[32] A. Ait Hssi, L. Atourki, N. Labchir, M. Ouafi, K. Abouabassi, A. Elfanaoui, A. Ihlal, S. Benmokhtar, K. Bouabid, High-quality Cu2O thin films via electrochemical synthesis under a variable applied potential, Journal of Materials Science: Materials in Electronics 31 (2020). https://doi.org/10.1007/s10854-020-02976-w.
[33] C. Ravichandiran, A. Sakthivelu, K. Deva Arun Kumar, R. Davidprabu, S. Valanarasu, A. Kathalingam, V. Ganesh, M. Shkir, H. Algarni, S. AlFaify, Influence of rare earth material (Sm3+) doping on the properties of electrodeposited Cu2O films for optoelectronics, Journal of Materials Science: Materials in Electronics 30 (2019) 2530–2537. https://doi.org/10.1007/s10854-018-0527-6.
[34] Y. Zhao, H. An, J. Feng, Y. Ren, J. Ma, Impact of Crystal Types of AgFeO2 Nanoparticles on the Peroxymonosulfate Activation in the Water, Environ Sci Technol 53 (2019). https://doi.org/10.1021/acs.est.9b00658.
[35] Q. Li, Y. Wang, Z. Chang, W. El Kolaly, F. Fan, M. Li, Progress in the treatment of copper(II)-containing wastewater and wastewater treatment systems based on combined technologies: A review, Journal of Water Process Engineering 58 (2024). https://doi.org/10.1016/j.jwpe.2023.104746.
[36] S. Zhu, X. Li, J. Kang, X. Duan, S. Wang, Persulfate Activation on Crystallographic Manganese Oxides: Mechanism of Singlet Oxygen Evolution for Nonradical Selective Degradation of Aqueous Contaminants, Environ Sci Technol 53 (2019). https://doi.org/10.1021/acs.est.8b04669.
[37] J. Yu, W. Qiu, H. Xu, X. Lu, J. Ma, D. Lu, Highly-efficient and stable MgCo2O4 spinel for bisphenol a removal by activating peroxymonosulfate via radical and non-radical pathways, Chemical Engineering Journal 421 (2021) 129498. https://doi.org/10.1016/j.cej.2021.129498.
[38] F. Wang, Y. Gao, H. Chu, Y. Wei, C.C. Wang, S.S. Liu, G. Liu, H. Fu, P. Wang, C. Zhao, The Pivotal Role of Selenium Vacancies in Defective FeSe2@MoO3 for Efficient Peroxymonosulfate Activation: Experimental and DFT Calculation, ACS ES and T Engineering 4 (2024). https://doi.org/10.1021/acsestengg.3c00195.
[39] Y. Gao, Y. Zhou, S.Y. Pang, J. Jiang, Y.M. Shen, Y. Song, J. Bin Duan, Q. Guo, Enhanced peroxymonosulfate activation via complexed Mn(II): A novel non-radical oxidation mechanism involving manganese intermediates, Water Res 193 (2021). https://doi.org/10.1016/j.watres.2021.116856.
[40] N.S. Shah, J. Iqbal, M. Sayed, A.A. Ghfar, J.A. Khan, Z.U.H. Khan, B. Murtaza, G. Boczkaj, F. Jamil, Enhanced solar light photocatalytic performance of Fe-ZnO in the presence of H2O2, S2O82−, and HSO5− for degradation of chlorpyrifos from agricultural wastes: Toxicities investigation, Chemosphere 287 (2022) 132331. https://doi.org/10.1016/j.chemosphere.2021.132331.
[41] Y. Guo, J. Long, J. Huang, G. Yu, Y. Wang, Can the commonly used quenching method really evaluate the role of reactive oxygen species in pollutant abatement during catalytic ozonation?, Water Res 215 (2022). https://doi.org/10.1016/j.watres.2022.118275.
[42] P. Shao, Y. Jing, X. Duan, H. Lin, L. Yang, W. Ren, F. Deng, B. Li, X. Luo, S. Wang, Revisiting the Graphitized Nanodiamond-Mediated Activation of Peroxymonosulfate: Singlet Oxygenation versus Electron Transfer, Environ Sci Technol 55 (2021).

https://doi.org/10.1021/acs.est.1c02042.
[43] H. Wang, W. Guo, Q. Si, B. Liu, Q. Zhao, H. Luo, N. Ren, Non-covalent doping of carbon nitride with biochar: Boosted peroxymonosulfate activation performance and unexpected singlet oxygen evolution mechanism, Chemical Engineering Journal 418 (2021). https://doi.org/10.1016/j.cej.2021.129504.
[44] Y. Gao, Q. Zhao, Y. Li, Y. Li, J. Gou, X. Cheng, Degradation of sulfamethoxazole by peroxymonosulfate activated by waste eggshell supported Ag2O-Ag nano–particles, Chemical Engineering Journal 405 (2021). https://doi.org/10.1016/j.cej.2020.126719.
[45] W. Tan, W. Ren, C. Wang, Y. Fan, B. Deng, H. Lin, H. Zhang, Peroxymonosulfate activated with waste battery-based Mn-Fe oxides for pollutant removal: Electron transfer mechanism, selective oxidation and LFER analysis, Chemical Engineering Journal 394 (2020). https://doi.org/10.1016/j.cej.2020.124864.
[46] T. Zhang, H. Zhu, J.P. Croué, Production of sulfate radical from peroxymonosulfate induced by a magnetically separable CuFe2O4 spinel in water: Efficiency, stability, and mechanism, Environ Sci Technol 47 (2013). https://doi.org/10.1021/es304721g.
[47] S.S. Gabr, M.F. Mubarak, M. Keshawy, I.E.T. El Sayed, T. Abdel Moghny, Linear and nonlinear regression analysis of phenol and P-nitrophenol adsorption on a hybrid nanocarbon of ACTF: kinetics, isotherm, and thermodynamic modeling, Appl Water Sci 13 (2023). https://doi.org/10.1007/s13201-023-02018-w.
[48] L. Wang, H. Zheng, C. Hu, H. Zeng, X. Ma, Q. Li, X. Li, S. Zhou, J. Deng, Novel UV-LED-driven photocatalysis-chlorine activation for carbamazepine degradation by sulfur-doped NH2-MIL 53 (Fe) composites: Electronic modulation effect and the dual role of chlorine, J Hazard Mater 464 (2024). https://doi.org/10.1016/j.jhazmat.2023.133037.
[49] J. Li, Y. Ren, F. Ji, B. Lai, Heterogeneous catalytic oxidation for the degradation of p-nitrophenol in aqueous solution by persulfate activated with CuFe2O4 magnetic nano-particles, Chemical Engineering Journal 324 (2017). https://doi.org/10.1016/j.cej.2017.04.104.
[50] Z. Li, J. Kang, Y. Tang, C. Jin, H. Luo, S. Li, J. Liu, M. Wang, C. Lv, The enhanced P-nitrophenol degradation with Fe/Co3O4 mesoporous nanosheets via peroxymonosulfate activation and its mechanism insight, J Alloys Compd 858 (2021). https://doi.org/10.1016/j.jallcom.2020.157739.

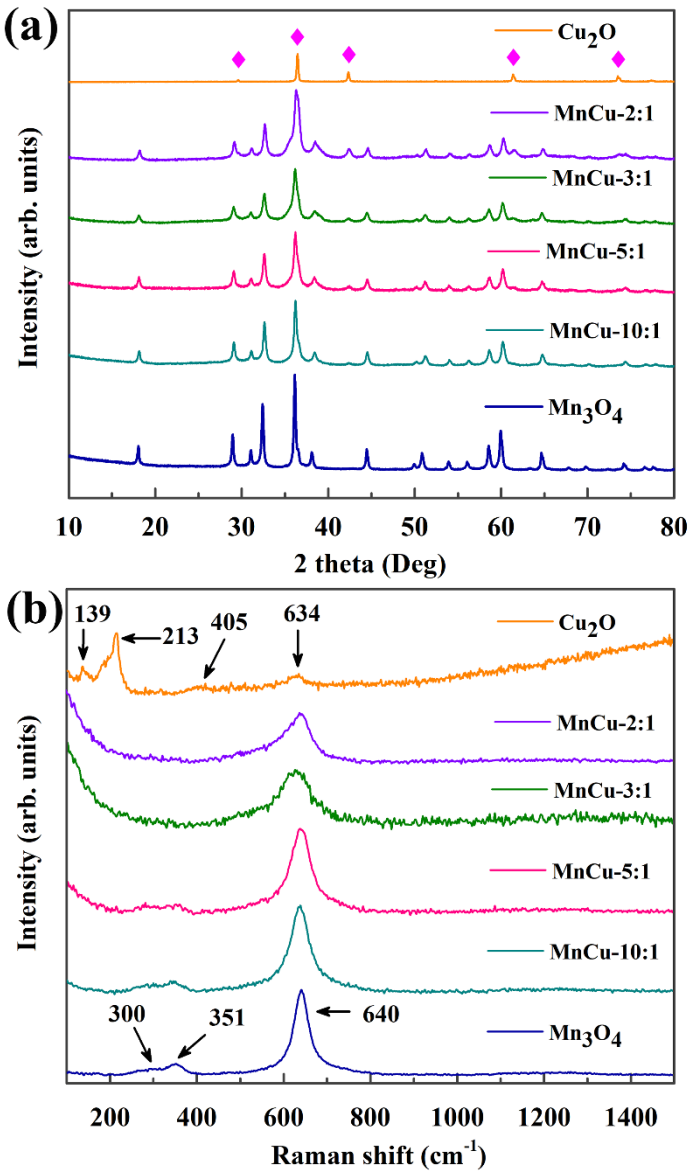


862

863 **Fig. 1.** (a) XRD pattern and (b) Raman spectra of $Mn_3O_4$, $Cu_2O$, and MnCu samples.

864

865

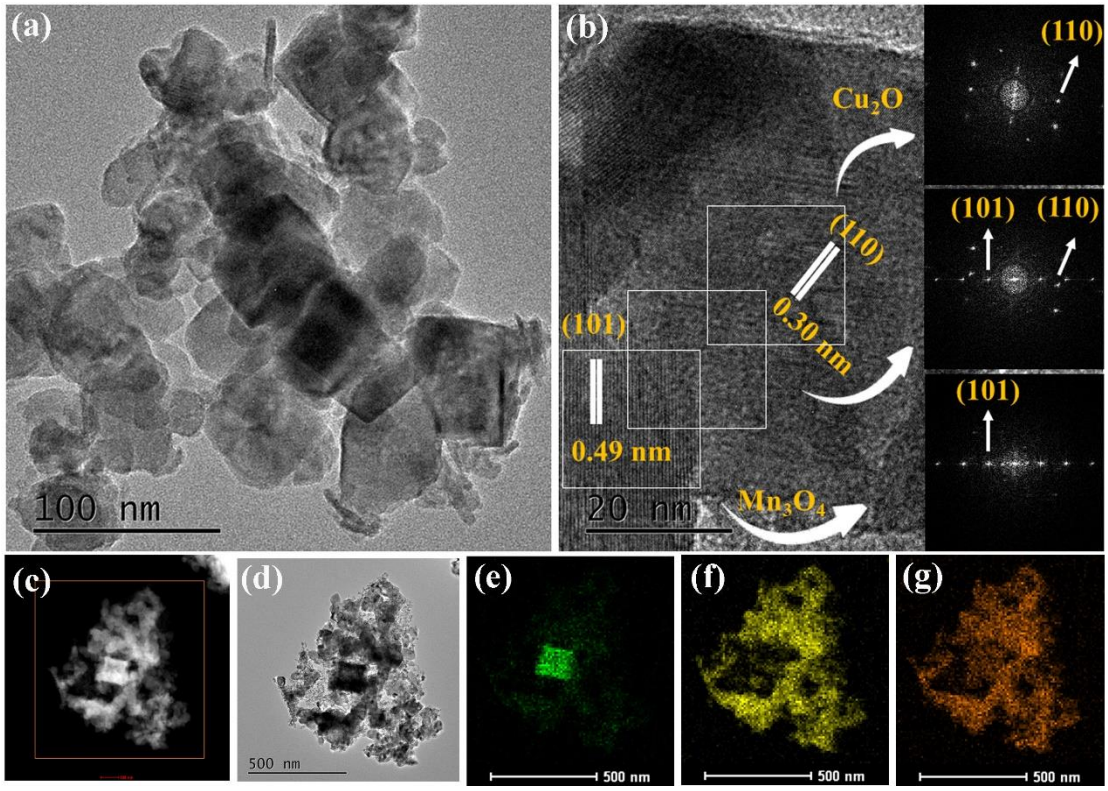


866

867 **Fig. 2**. Structural characterizations of the MnCu-5:1 catalyst, (a) TEM image, (b) FFT

868 inset in HRTEM images, (c) HAADF, (d) BF, and the corresponding EDX mapping

869 images for (e) Cu, (f) Mn, (g) O of MnCu-5:1 catalyst.

870

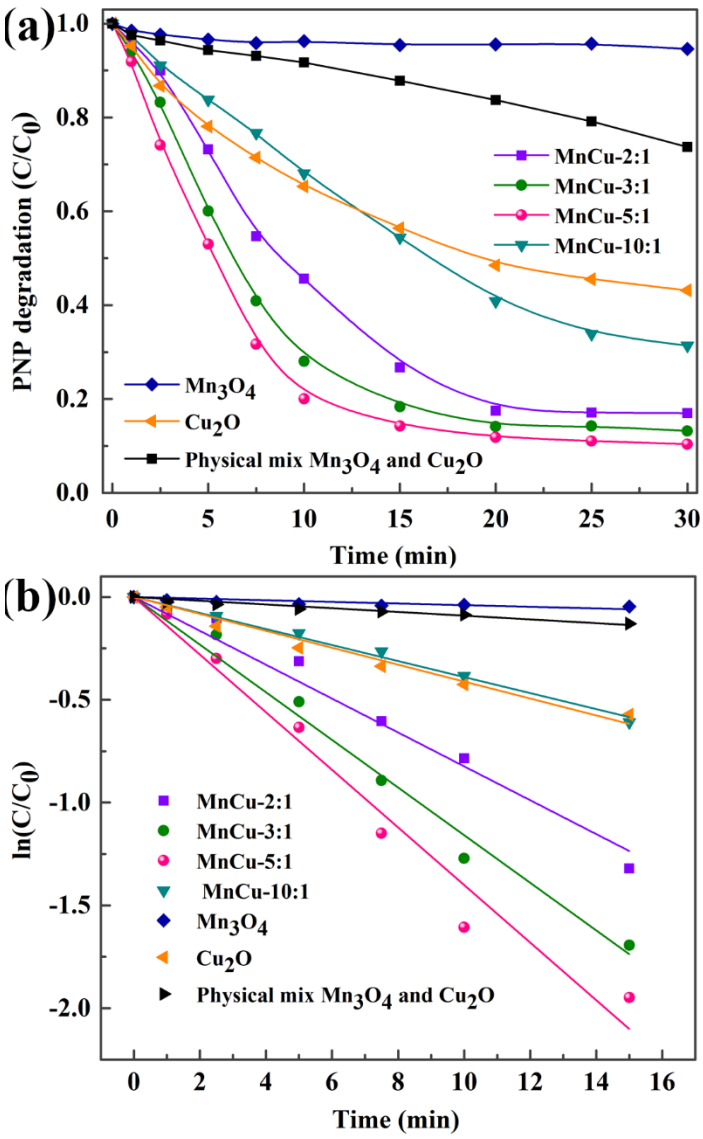


871

872 **Fig. 3.** (a) PNP degradation on Mn/Cu-based catalysts/PMS system, (b) kinetic model

873 of catalytic PNP reactions. Reaction conditions: Catalyst 0.2 g/L, PMS 0.64 mM, pH

874 8.2, PNP 50 μM, and temperature 25 ˚C.

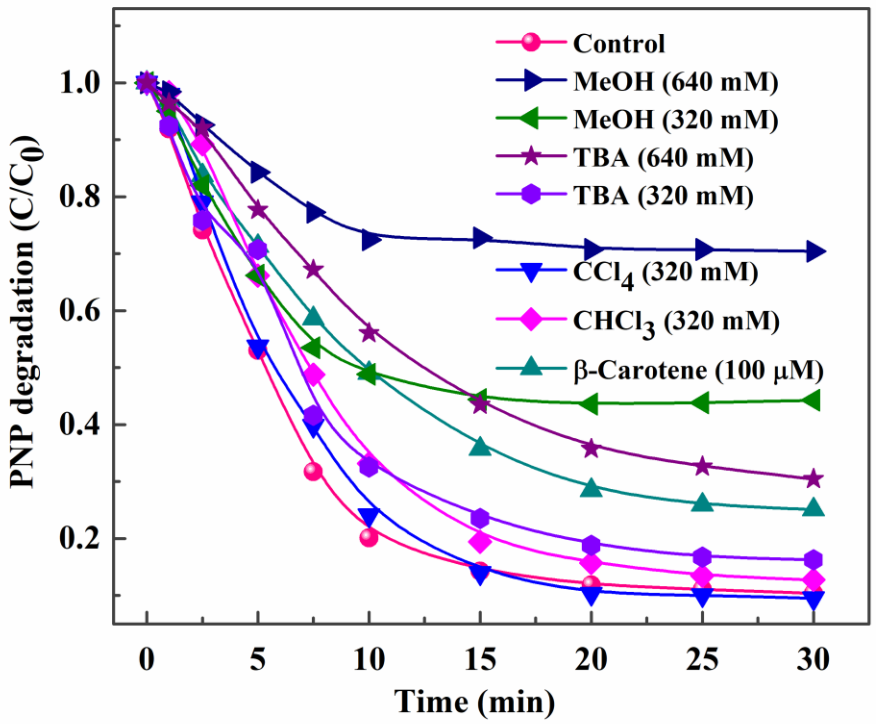


875

876 **Fig. 4.** Inhibition of MeOH, TBA, $CCl_4$, $CHCl_3$ and β-Carotene on the PNP degradation

877 by MnCu-5:1/PMS. Reaction conditions: Catalyst 0.2 g/L, PMS 0.64 mM, pH 8.2,

878 PNP 50 μM, and temperature 25 ˚C.

879

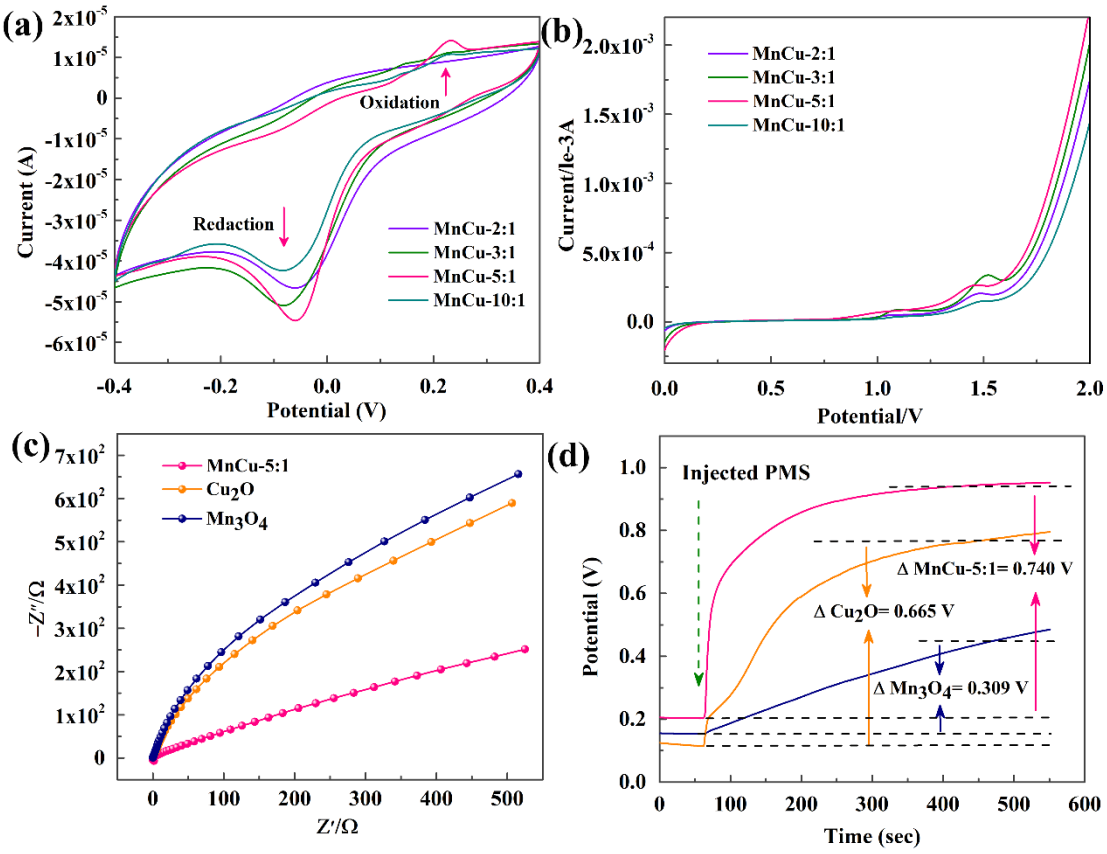


**Fig. 5.** (a) CVs, and (b) LSV curves obtained on MnCu-10:1, MnCu-5:1, MnCu-3:1, and MnCu-2:1 as electrodes in a mixed solution of $Na_2SO_4$ (0.1 M), PMS (0.64 mM), and Scan rate = 50 mV $s^{-1}$. (c) EIS Nyquist plots, and (d) OCP curve of $Mn_3O_4$ and $Cu_2O$, and MnCu-5:1 as electrodes in a solution of $Na_2SO_4$ (0.1 M).

887

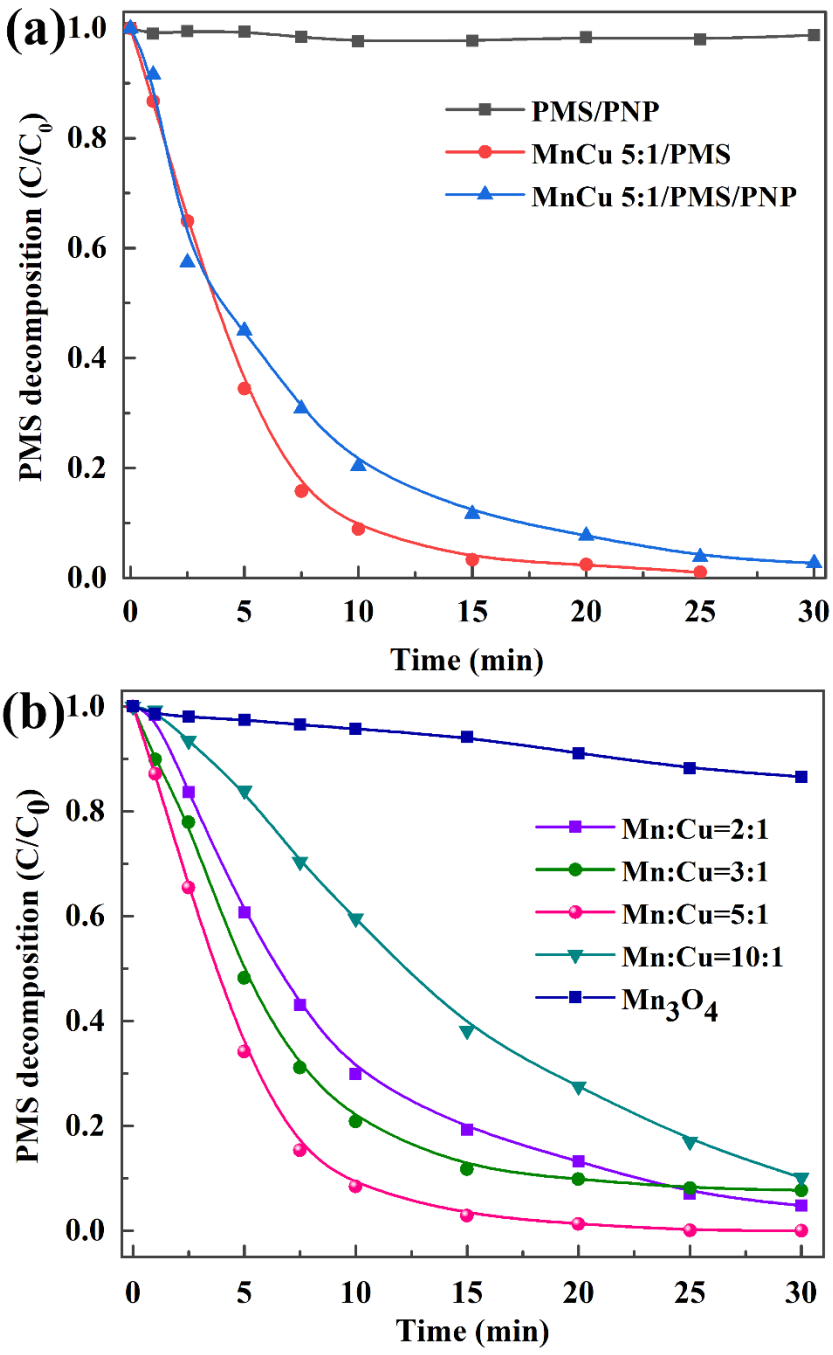


888

889 **Fig. 6.** (a) PMS decomposition on various systems, and (b) PMS decomposition on

890 different catalysts. Reaction conditions: Catalyst 0.2 g/L, PMS 0.64 mM, pH 8.2, PNP

891 50 μM, and temperature 25 ˚C.

892

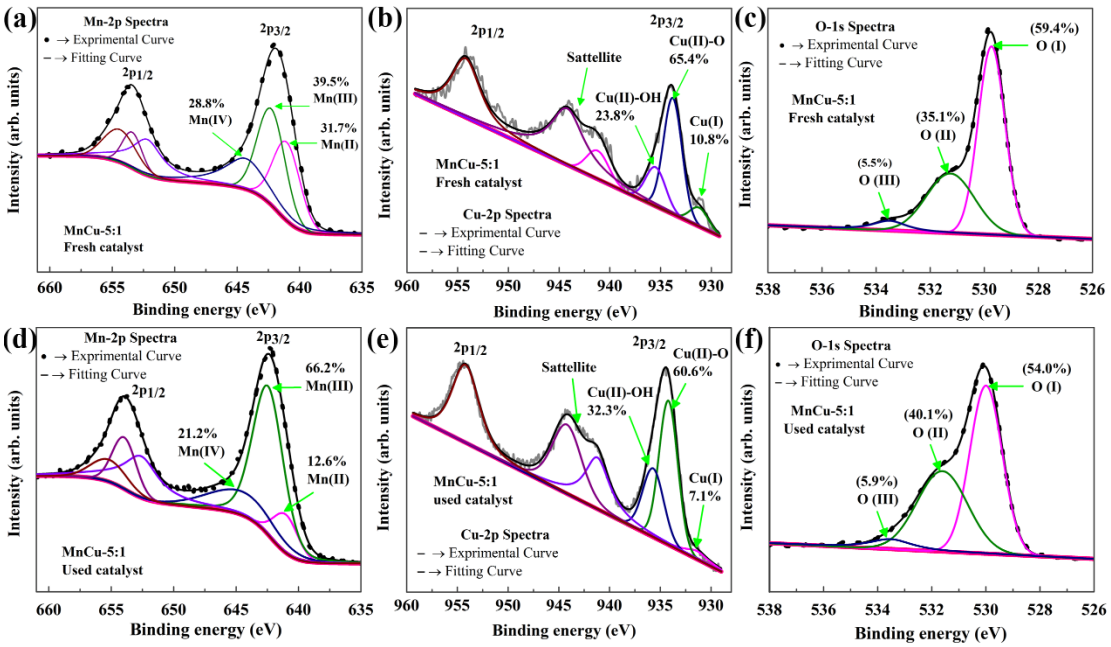


**Fig. 7.** (a and d) XPS spectra of Mn 2p fresh and used catalyst, (b and e) XPS spectra of Cu 2p fresh and used catalyst and (c and f) XPS spectra of O 1s fresh and used catalyst for the MnCu-5:1.

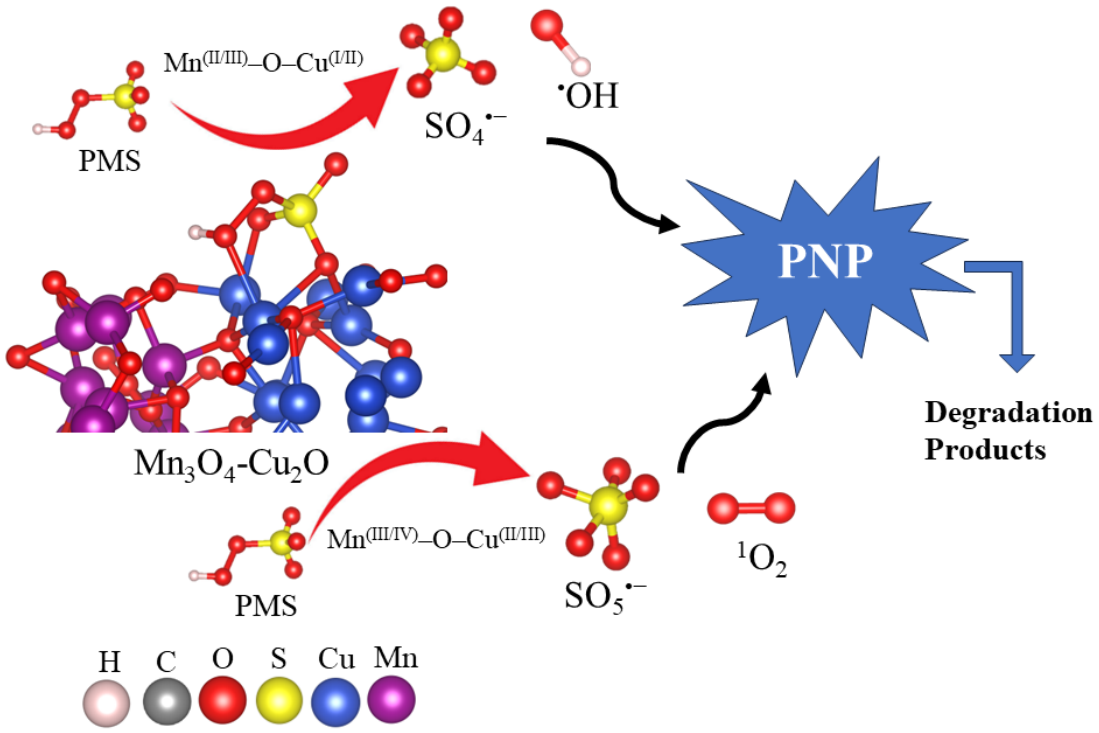


900

901 **Scheme 1.** A possible reaction mechanism over the $Mn_3O_4$-$Cu_2O$/PMS system for PNP

902 degradation.

903

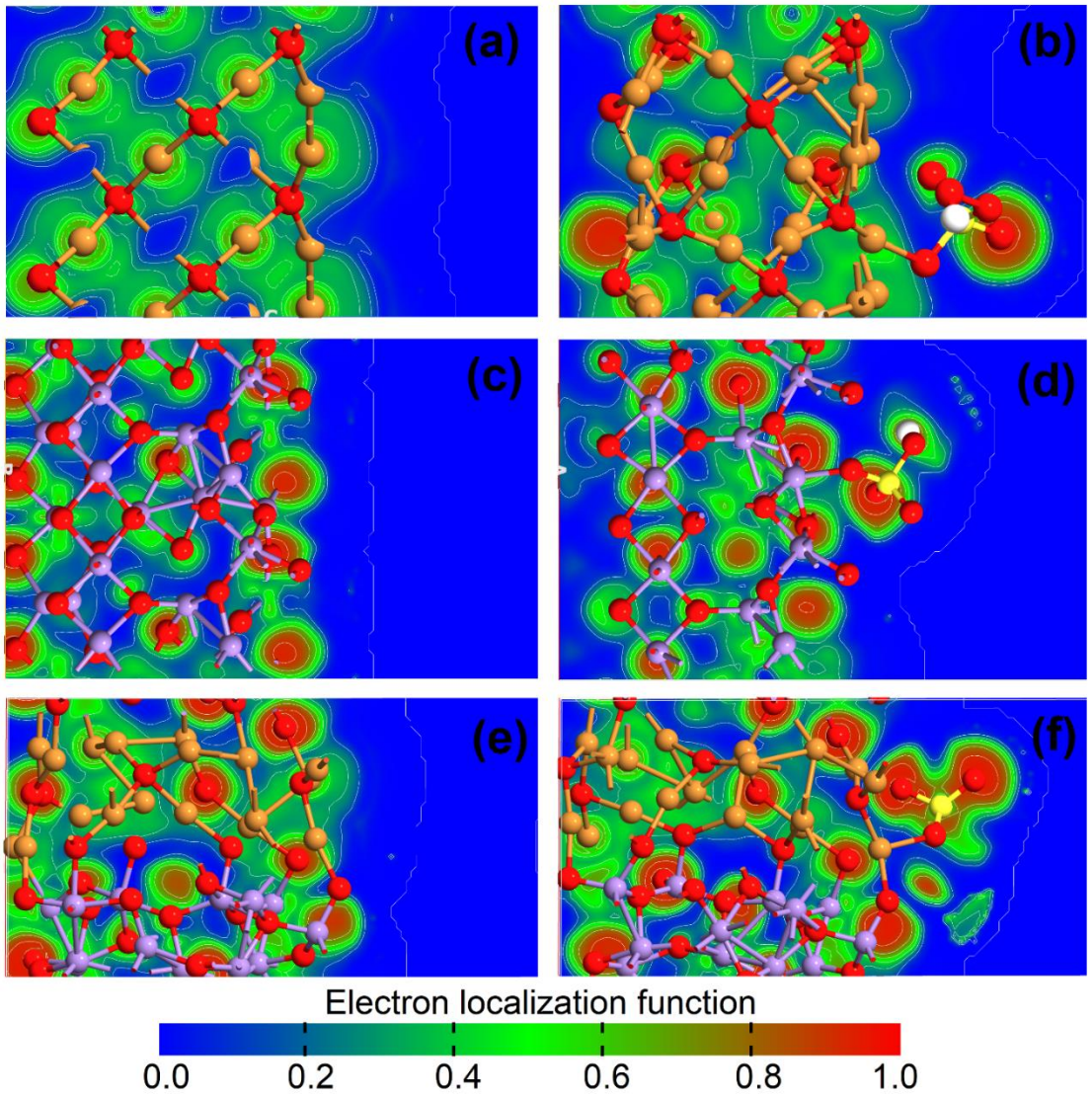


**Fig. 8.** Electron localization function maps of (a) $Cu_2O$, (b) $Mn_3O_4$, and (c) $Mn_3O_4$-$Cu_2O$ composite, along with their PMS interacted (d) $Cu_2O$/PMS, (e) $Mn_3O_4$/PMS, and (f) $Mn_3O_4$-$Cu_2O$/PMS system.

910

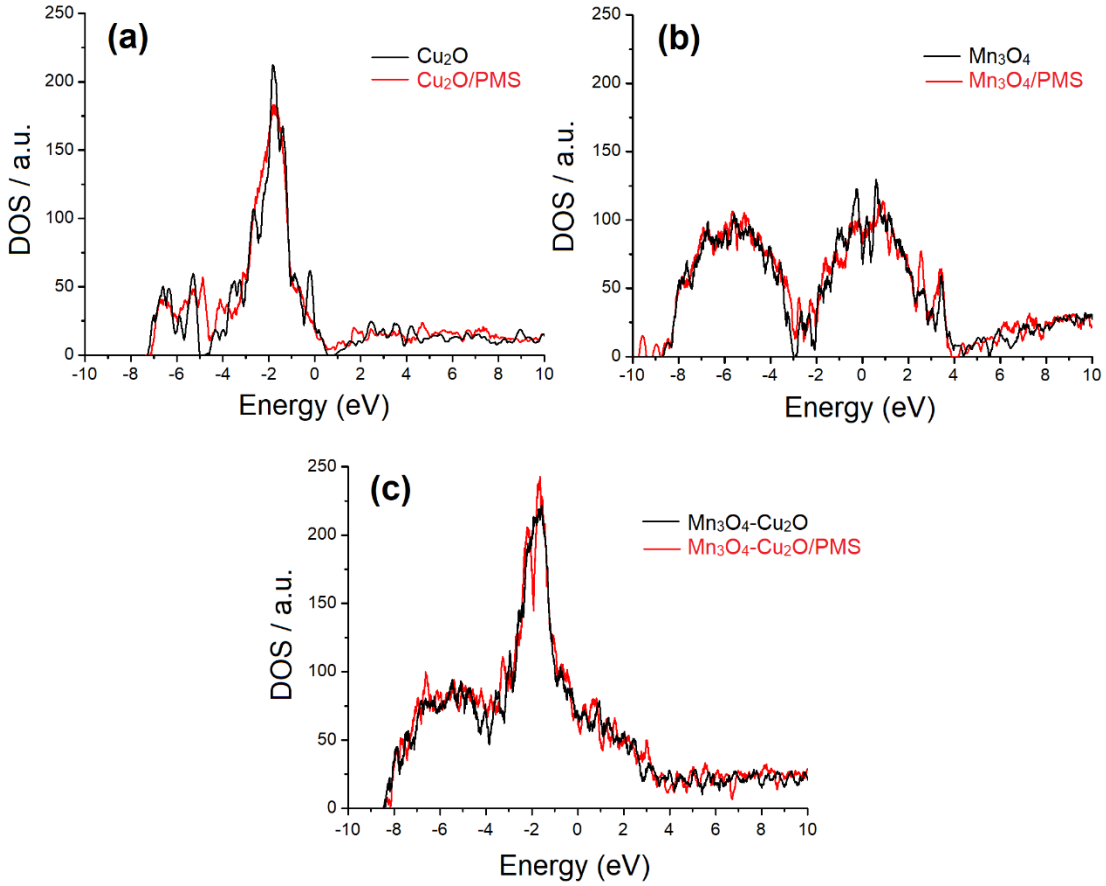


911

912 **Fig. 9.** Density of states plots of (a) $Cu_2O$, (b) $Mn_3O_4$, and (c) $Mn_3O_4$-$Cu_2O$ composite,

913 with and without PMS interaction. The Fermi energy is set to zero.

914

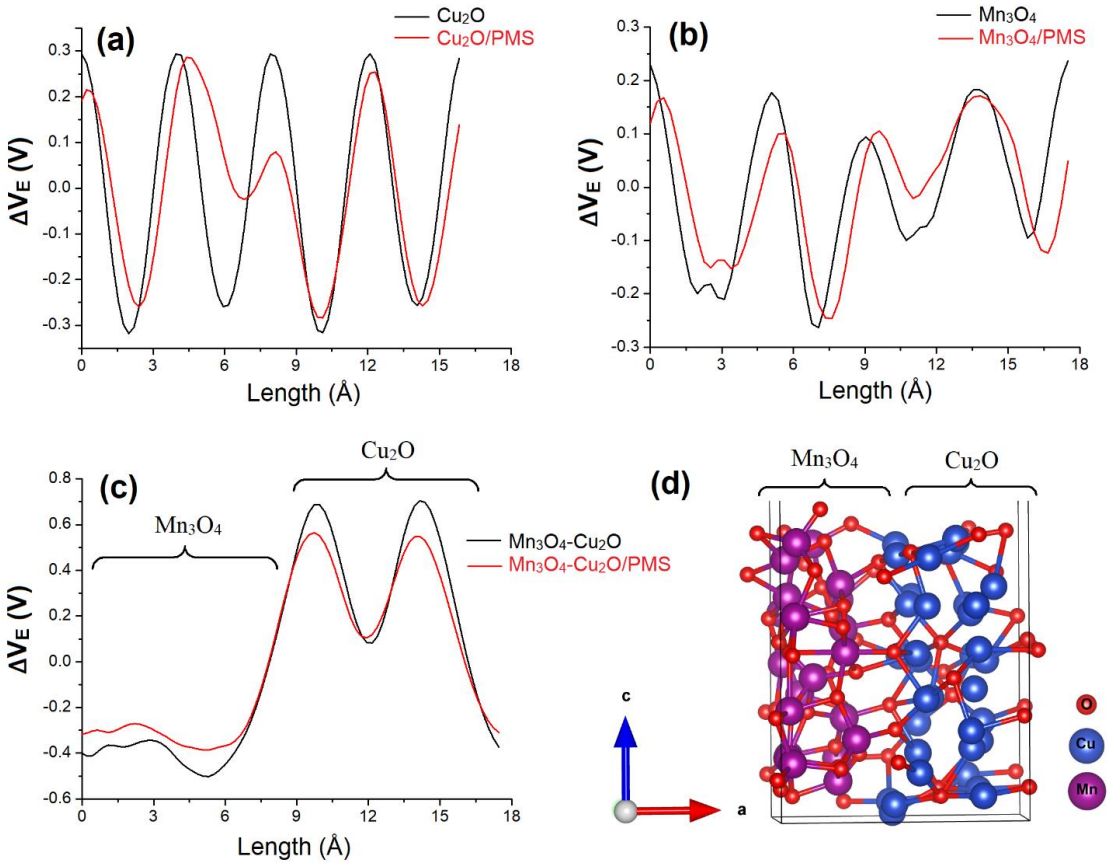


**Fig. 10.** 2D electrostatic difference potential plots of (a) $Cu_2O$, (b) $Mn_3O_4$, and (c) $Mn_3O_4$-$Cu_2O$ composite, with and without PMS interaction. All these plots are along a-axis. (d) is provided to clearly understand the directions of atoms in the $Mn_3O_4$-$Cu_2O$ composite.